

**СПЕКТРОСКОПИЧЕСКИ И/ИЛИ СТРУКТУРНО ИНТРИГУЮЩИЕ ФТАЛОЦИАНИНЫ
И РОДСТВЕННЫЕ СОЕДИНЕНИЯ. ЧАСТЬ 2. МОНОМЕРНЫЕ СИСТЕМЫ**

Н. Кобаяши

Нагао Кобаяши

Кафедра химии и материалов, факультет текстильных наук и технологии, университет Шиншу, Уэда, 386-8567, Япония

E-mail: nagaok@shinshu-u.ac.jp, nagaokobayashi.c3@tohoku.ac.jp

Представлена вторая часть серии обзорных работ по свойствам некоторых синтетически и спектроскопически интересных исследований нашей группы за период 2007-2017 гг. В частности, приведены примеры анализа спектроскопических данных в сочетании с расчетами методом молекулярных орбиталей. Мы использовали в основном спектроскопические методы электронного поглощения и естественного и магнитного кругового дихроизма, периодически применяя флуоресценцию, фосфоресценцию и ЭПР с временным разрешением. Теоретически проанализированы спектры $(4n + 2)$ π систем, а также некоторые $4n\pi$ антиароматических систем, что помогает читателю интерпретировать спектральные данные. В первой и второй частях этого обзора рассматриваются мономерные системы, а в третьей - тримерные и тетрамерные системы.

Ключевые слова: фталоцианины, энергия, МО, строение, спектры

**SPECTROSCOPICALLY AND/OR STRUCTURALLY INTRIGUING PHTHALOCYANINES
AND RELATED COMPOUNDS. PART 2. MONOMERIC SYSTEMS**

N. Kobayashi

Nagao Kobayashi

Department of Chemistry and Materials, Faculty of Textile Science and Technology, Shinshu University, Ueda, 386-8567, Japan

E-mail: nagaok@shinshu-u.ac.jp, nagaokobayashi.c3@tohoku.ac.jp

The second part of the series of review papers on the properties of some synthetically and spectroscopically interesting studies of our group for the period 2007-2017 is presented. In particular, examples of the analysis of spectroscopic data in combination with calculations by the molecular orbitals method are given. We mainly used spectroscopic methods of electron absorption and natural and magnetic circular dichroism, periodically applying fluorescence, phosphorescence and ESR with a time resolution. The spectra of $(4n + 2)$ π systems, as well as some $4n\pi$ antiaromatic systems, are analyzed theoretically, which helps the reader to interpret the spectral data. In the first and the second parts of this review monomer systems are considered, and in the third - trimeric and tetrameric systems.

Key words: phthalocyanines, energy, MO, structure, spectra

Для цитирования:

Кобаяши Н. Спектроскопически и/или структурно интригующие фталоцианины и родственные соединения. Часть 2. Мономерные системы. *Изв. вузов. Химия и хим. технология*. 2019. Т. 62. Вып. 8. С. 4–25

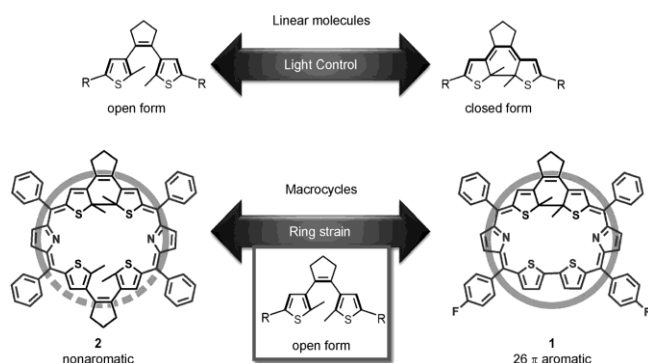
For citation:

Kobayashi N. Spectroscopically and/or structurally intriguing phthalocyanines and related compounds. Part 2. Monomeric systems. *Izv. Vyssh. Uchebn. Zaved. Khim. Khim. Tekhnol.* 2019. V. 62. N 8. P. 4–25

2-4 Ring-Expanded Systems**Core-Modified Rubyrins Containing Dithienylethene Moieties [1]**

Aromaticity is a fundamental concept of chemical structure and bonding, which describes the enhanced stability that is derived from the delocalization of π -electrons in cyclic conjugated macrocycles. Although aromaticity cannot be quantified directly by experiment, it can be analyzed by studying the molecular and electronic structures, and the external magnetic field induced diamagnetic ring current. Theoretical calculations such as nucleus-independent chemical shift (NICS) and anisotropy of the current-induced density (ACID) can be used to determine the extent to which a novel macrocycle is aromatic [2]. Typically, porphyrins can be regarded as aromatic molecules following Hückel's $(4n+2)$ rule as 18 π -electrons are delocalized along the inner ligand perimeter. Core-modified and ring-expanded porphyrins have been intensively studied because of their suitability for various applications. Extent of macrocyclic aromaticity is closely related to the number of π -electrons and the topology of the molecular structure. The aromatic character can be fine-tuned through protonation, by modifying the solvent polarity and coordination environment, and by incorporating novel heterocyclic moieties as building blocks [1].

Dithienylethene (DTE) can exhibit switchable properties in response to certain external stimuli such as light, redox potential, oxidation/reduction, and the presence of ions (Scheme 1).



Scheme 1. Schematic representation of the cycloreversion of DTE (top) and structures of rubyrins containing one (**1**) and two (**2**) DTE units (bottom)

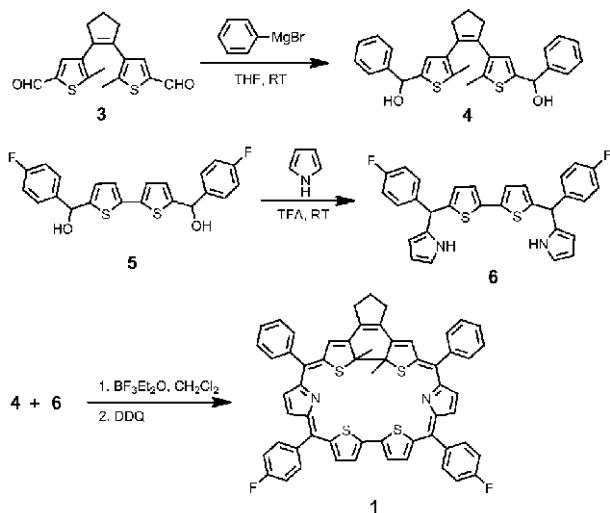
Схема 1. Схематическое представление цикловерсии DTE (вверху) и структур рублиринов, содержащих одну (**1**) и две (**2**) единицы DTE (внизу)

In the open form of DTE, two thiophene units are linked at their β -positions through a cyclopentene moiety, and thus the conjugation pathway (indicated by alternating single and double bonds) is not planar. In the closed form, the two α -positions of the thiophene units are linked directly, leading to the extension of the π -conjugation system over the entire DTE moiety. The unique structural flexibility inspired us to think about introducing a DTE unit into a macrocycle. Core-modified rubyrins were selected so that the aromaticity of porphyrinoids can be studied further. Porphyrinoid macrocycles containing one (**1**) and two (**2**) DTE moieties were designed, synthesized, and characterized (Scheme 1). The noteworthy findings were that firstly, even under dark conditions, the embedded DTE moiety of the compound with one DTE moiety exists solely in the closed form, suggesting the formation of a very stable aromatic macrocycle with a 26 π -electron system. Secondly, the optical and redox properties of **1** differ markedly from those of conventional core-modified rubyrins with a 26 π -electron system. Thirdly, due to the constraints imposed by the geometry of the inner perimeter of the macrocycle, the rubyrin with two embedded DTE units (i.e. **2**) contains one closed and one open moiety and retains nonaromatic properties.

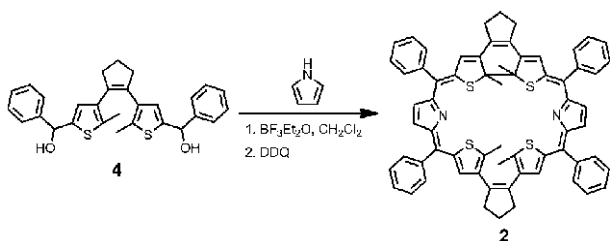
The key step in the short synthesis of **1** was the coupling of diol **4** and modified tetrapyrrole **6** (Scheme 2). Diol **4** was prepared by the double Grignard reaction of **3**, which was synthesized according to literature procedures [3]. The other coupling component, compound **6**, was obtained by reacting **5** [4] with excess pyrrole in the presence of trifluoroacetic acid (TFA). Finally, rubyrin **1** was prepared by the reaction of compounds **4** and **6** under Lindsey reaction conditions [5]. Core-modified rubyrin **2** was similarly obtained by the reaction of **4** and pyrrole (Scheme 3).

The structure of **1** was unambiguously elucidated by single crystal X-ray analysis (not shown). The ^1H NMR spectra of **1** and **2** were recorded in CD_2Cl_2 for comparison. In **1**, the signal of the thiophene methyl protons, which lie inside the conjugated macrocycle, was detected at high field ($\delta = -0.27$ ppm), while the thiophene protons of the DTE moiety appeared as a singlet at $\delta = 7.56$ ppm. In **2**, the chemical shifts of the thiophene methyl protons ($\delta = 2.01$ (6 H) and 2.18 (6 H)

ppm) and the thiophene protons ($\delta = 5.78$ (2H) and 6.85 (2H) ppm) of the DTE moiety are significantly different from those of **1**, indicating that there are two different types of methyl and DTE thiophene protons, as shown in the structure of **2**.



Scheme 2. Synthesis of core-modified ruyirin **1**
Схема 2. Синтез ядро-модифицированного руйирин **1**



Scheme 3. Synthesis of core-modified ruyirin **2**
Схема 3. Синтез ядро-модифицированного руйирин **2**

In order to disclose the conjugation pathways of **1** and **2**, the ACID (anisotropy of the induced current density) was calculated at the B3LYP/6-31G* level of theory (Fig. 1). There is a distinct diatropic ring current, which is revealed through numerous current density vectors on the isosurface, in the periphery of **1** (red line, clockwise). In contrast, there are only local currents (in benzene, pyrrole, and thiophene rings) in **2**. At a higher isosurface value there is a continuous isosurface in **1**. In **2**, however, the delocalization is interrupted. When this is combined with the bond length data for the **1** macrocycle from X-ray analysis (not shown), it is clearly evident that **1** has an aromatic 26 π -electron system. In contrast, there is no ring current on the outer ring periphery of **2**, as would be anticipated based on the ^1H NMR measurements. The π -system of **2** is clearly nonaromatic.

Molecular orbital (MO) and time-dependent (TD)-DFT calculations have been carried out for **1** and

2 (Figs. 2 and 3). Although alternating single and double bonds cannot be drawn for the “open-form” structure of **2** (Scheme 1), when viewed in the context of molecular orbital theory, the spectroscopic properties can still be analyzed using theoretical frameworks that have been derived for conjugated macrocycles. First, it is noteworthy that the nodal patterns of the HOMO and HOMO-1 and also the LUMO and LUMO+1 of **1** are consistent with what would be anticipated for a heteroaromatic 26 π -electron porphyrinoid, since six angular nodal planes are predicted for the HOMO level and seven for the LUMO level due to an $M_L = 0, \pm 1, \pm 2, \dots, \pm 11, \pm 12, 13$ sequence in terms of ascending energy for the MOs derived from a parent $\text{C}_{26}\text{H}_{26}$ aromatic hydrocarbon perimeter with D_{26h} symmetry.

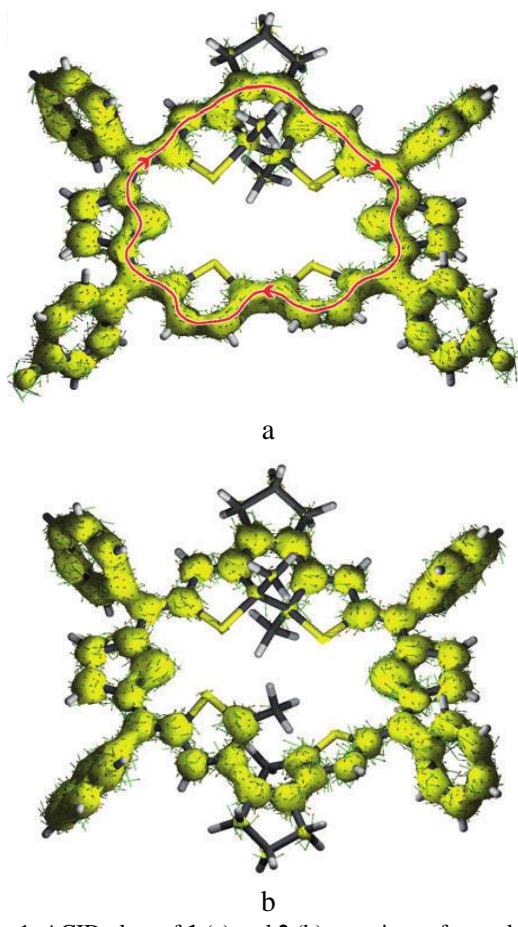


Fig. 1. ACID plots of **1** (a) and **2** (b) at an isosurface value of 0.065. The external magnetic field is applied orthogonal to the macrocycle plane with its vector pointing towards the viewer. Current density vectors (green lines and red conics) are plotted onto the ACID isosurface (Fig. 1 in color see <http://journals.isuct.ru/ctj/article/view/1520>)

Рис. 1. Графики кислотности **1** (a) и **2** (b) при изоповерхностном значении 0,065. Внешнее магнитное поле прикладывается ортогонально к плоскости макроцикла с вектором, направленным на зрителя. Векторы плотности тока (зеленые линии и красные конические сечения) нанесены на изоповерхности (Рис. 1 в цвете смотри <http://journals.isuct.ru/ctj/article/view/1520>)

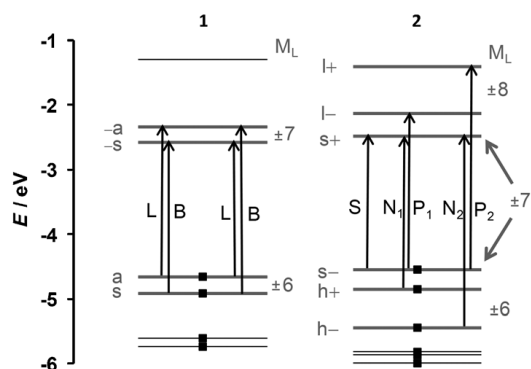


Fig. 2. The predicted energies of the frontier π -MOs based on the X-ray structure of **1** and the optimized geometry of **2** at the B3LYP/6-31G* level of theory. Black squares are used to denote occupied MOs. Vertical arrows denote the one-electron transitions associated with the L and B bands of Michl's $4n+2$ perimeter model [6, 7] and the S, $N_{1/2}$, and $P_{1/2}$ bands of the $4n$ perimeter model [8-11]

Рис. 2. Предсказанные энергии граничных π -МО, основанные на рентгеновской структуре **1**, и оптимизированная геометрия **2** на уровне теории B3LYP / 6-31G*. Черные квадраты используются для обозначения занятых МО. Вертикальными стрелками обозначены одноэлектронные переходы, связанные с полосами L и B модели $4n+2$ периметра Мишля [6, 7] и полосами S, $N_{1/2}$ и $P_{1/2}$ модели периметра $4n$ [8-11]

Michl and co-workers have demonstrated that this is the pattern that would normally be anticipated for a heteroaromatic $4n+2$ π -system with 26 atoms and 26 π -electrons [6, 7]. Since only relatively minor energy splittings (the Δ HOMO and Δ LUMO values to use Michl's terminology) are predicted for the four frontier π -MOs derived from the HOMO and LUMO of the parent perimeter, almost fully forbidden L bands and strongly allowed B bands are expected to dominate the UV/Vis absorption spectrum, with pairs of coupled Faraday B terms of opposite signs anticipated in the MCD spectrum in each case. The bands in the 450-600 and 650-850 nm ranges (Fig. 3) can be assigned to the B and L transitions based on the TD-DFT calculations and the sign sequences observed in the MCD spectrum.

Due to the presence of the "open-form" DTE unit, the optical properties of the π -system of **2** can be readily interpreted using Michl's $4N$ perimeter model (Fig. 2) [8-11]. Six frontier π -MOs derived from the HOMO, SOMO, and LUMO of the parent hydrocarbon perimeter (referred to by Michl as the h_- , h_+ , s_- , s_+ , L , and l_+ MOs) have six, seven, and eight angular nodal planes (not shown), respectively, and play the key role in the low-energy singlet electronic states. The intensities of the MCD bands are an order of magnitude weaker than those of **1**, since the induced excited-state magnetic moments are very weak due to the absence of a heteroaromatic conjugation pathway [12, 13]. The

lowest energy band is associated with the $s_- \rightarrow s_+$ transition, which is of an intrashell nature. The absorption and hence also the MCD intensity of the S band is usually predicted to have near-zero intensity. The weak tail of intensity in the 700-850 nm region can be assigned to this transition (Fig. 3). The other spin-allowed electronic transitions within the model are inter-shell, being derived from HOMO \rightarrow SOMO and SOMO \rightarrow LUMO one-electron transitions (Fig. 2). Two weak (N_1 , N_2) and two strong (P_1 , P_2) electric-dipole transitions are predicted on this basis, which can be readily assigned based on the TD-DFT calculation to the more intense coupled pairs of Faraday B terms in the 450-650 nm range.

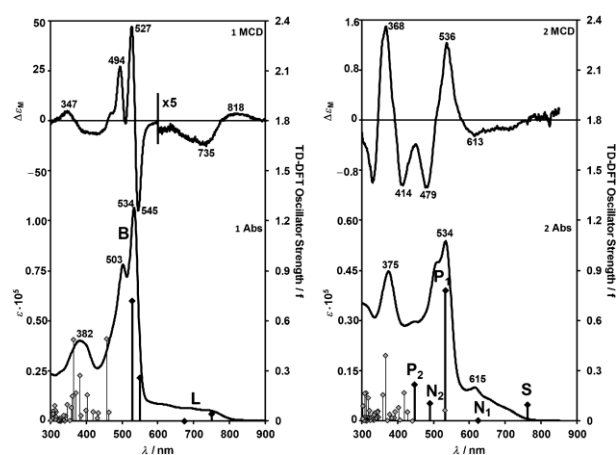


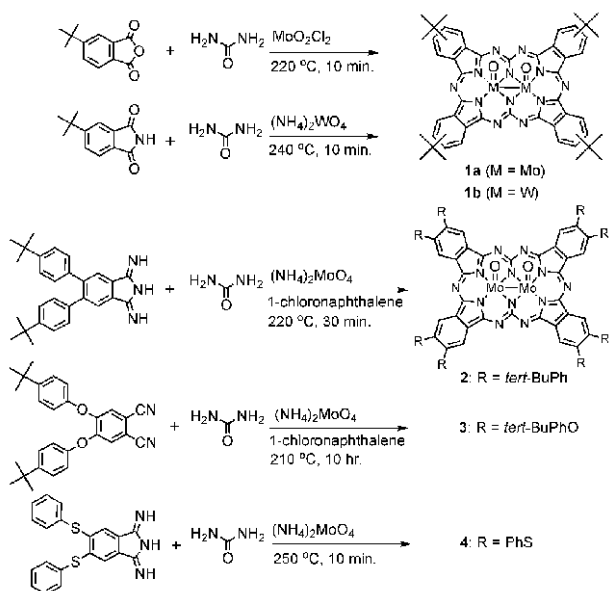
Fig. 3. The observed electronic absorption spectra of **1** and **2**, and the calculated TD-DFT (diamonds) oscillator strengths based on the X-ray structure of **1** and the optimized geometry of **2** at the B3LYP/6-31G* level of theory plotted against the primary and secondary vertical axes, respectively. Black and light gray diamonds are used to highlight the L and B bands from Michl's $4n+2$ perimeter model [6, 7] and the S, $N_{1/2}$, and $P_{1/2}$ bands from the $4n$ perimeter model [8-11]. Рис. 3. Наблюдаемые электронные спектры поглощения **1** и **2**, и рассчитанные значения сил осцилляторов по TD-DFT (алмазы) на основе рентгеновской структуры **1** и оптимизированной геометрии **2** на уровне теории B3LYP / 6-31G*, нанесенные на график относительно первичной и вторичной вертикальных осей, соответственно. Черные и светло-серые ромбы используются для выделения полос L и B из модели периметра $4n+2$ Мишля [6, 7] и полос S, $N_{1/2}$ и $P_{1/2}$ из модели периметра $4n$ [8-11]

In summary, a heteroaromatic core-modified rubein bearing one dithienylethene moiety (**1**) has been successfully synthesized and characterized for the first time, along with a nonaromatic macrocycle containing both an "open-form" and a "closed-form" dithienylethene moiety (**2**). An analysis of the MCD spectral data and the TD-DFT and ACID calculations clearly demonstrated that the π -systems of **1** and **2** are aromatic and nonaromatic, respectively. The use of a dithienylethene moiety as a building block, therefore, offers a new vista of opportunities for tuning the aromaticity of ring-expanded core-modified porphyrins.

b) Rectangular-Shaped Expanded Phthalocyanines with Two Central Metal Atoms [14]

Although more than 300 X-ray structures have been reported for metallo-Pcs, [15] SubPcs, and Super-Pcs, all of these compounds contain isoindole rings connected by aza nitrogen atoms whether they are monomeric, dimeric, or oligomeric, and no other complex types have been reported from the Pc formation reactions [16, 17]. In this article, we provide the first report of a completely new type of Pc complex containing two metal ions that is obtained under normal Pc formation reaction conditions in the presence of molybdenum and tungsten salts.

In a similar manner to normal Pc formation reactions, a mixture of phthalic anhydride or phthalimide and excess urea (and occasionally a trace amount of 1-chloronaphthalene for ease of stirring; see Scheme 4) was heated in the presence of a molybdenum [MoO_2Cl_2 or $(\text{NH}_4)_2\text{MoO}_4$] or tungsten salt [$(\text{NH}_4)_2\text{WO}_4$] at 210–250 °C for 10–30 min, and the products were purified by chromatography using silica gel followed by a size-exclusion column. After removal of greenish-blue bands containing normal Pcs, another band with a brown color was collected, and strong electronic absorption bands beyond 900 nm were detected. The yields were always higher for molybdenum salts (max. 8.3%) than for tungsten salts (less than 2.0%). The tungsten derivatives tended to decompose during column chromatography. Although the yield was low, a similar compound (**3**) was obtained even when phthalonitrile and urea were used as the starting materials.



Scheme 4. Synthesis of **1-4**
Схема 4. Синтез соединений **1-4**

The absorption spectra of each of these compounds did not change upon storage for up to a year so

long as they were kept in the dark in the solid state. This demonstrates that these compounds are reasonably stable. However, when the complexes were dissolved in solution or stored under direct light, they decomposed more slowly than ZnPc but more quickly than CuPc.

All of the brown compounds with intense absorption bands beyond 900 nm were subjected to analysis by mass spectrometry (MS). The high-resolution MS (HR-MS) spectra and calculated isotopic distribution patterns provided a reasonable match for the compounds with two atoms of molybdenum (**1a**, **2**, and **3**) or tungsten (**1b**). To provide a further confirmation of the number of nitrogen atoms, ^{15}N -labeled **1a** was synthesized using ^{15}N -labeled urea. The parent peak was observed by HR-MS at m/z 1076.1677 [$\text{M}^+ + \text{Na}$], while m/z 1076.1678 was calculated for $\text{C}_{50}\text{H}_{48}\text{Mo}_2^{15}\text{N}_{12}\text{O}_2\text{Na}$. The theoretical isotopic distribution pattern matched the experimental one almost perfectly. When the mass data obtained for **4** were taken into consideration, all of the mass data could be successfully reproduced only when 12 nitrogen atoms, two oxygen atoms, and two molybdenum or tungsten atoms were included.

The crystal structure of **2** (Fig. 4) reveals that the macrocycle comprises four isoindole rings linked by two methanetriamine moieties and contains two Mo ions in its central cavity. Two oxygen atoms are connected to each Mo ion from the same direction as axial ligands (i.e., a *cis* isomer).

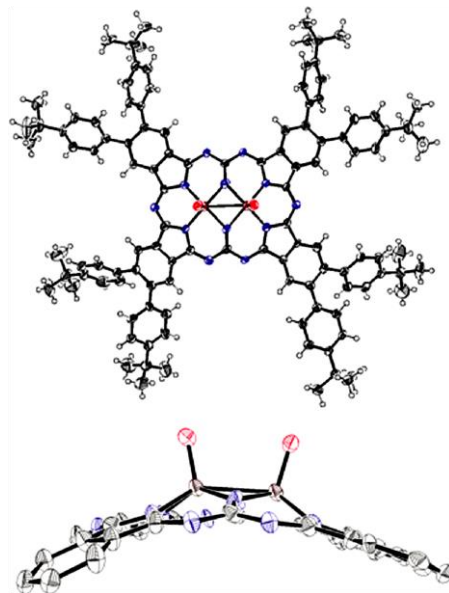


Fig. 4. X-ray crystal structure of **2**: (top) top view; (bottom) side view. The thermal ellipsoids are scaled to the 50% probability level. For clarity, H atoms and substituents have been omitted in the side view
Рис. 4. Рентгенокристаллическая структура **2**: (сверху) вид сверху; (снизу) вид сбоку. Тепловые эллипсоиды масштабируются до уровня вероятности 50%. Для ясности, атомы H и заместители были опущены на виде сбоку

The Mo–O bonding distance of 1.66 Å in the crystal structure is in the range of lengths for Mo=O double bonds [18]. The interatomic distance between the two Mo ions is 2.64 Å, which corresponds to the distance of a Mo–Mo single bond [19]. Each Mo ion is further coordinated by two pyrrole nitrogen atoms and two amino nitrogen atoms of the macrocycle (**5A** in Fig. 5). The overall molecular structure of **2** adopts a dome shape. The dihedral angles formed by the isoindole moieties are 39° on average. The Mo ions lie out of the macrocyclic plane. No significant bond-length alternation was observed for the C–N and C–C bonds of the core structure of **2**, as would be anticipated for a heteroaromatic π system. This pattern is generally observed in the crystal structures of Pc congeners. On the basis of the MS and ^1H NMR data described below, the only other isomer that could be formed would contain two nitride-type nitrogen atoms connected at the axial positions and two oxygen atoms in turn residing at the *meso* positions to coordinate each Mo ion along with two pyrrole nitrogen atoms in a square planar fashion (**5B** in Fig. 5). A detailed analysis of both structures revealed that the thermal ellipsoids were properly solved for the structure **5A** in Fig. 5.

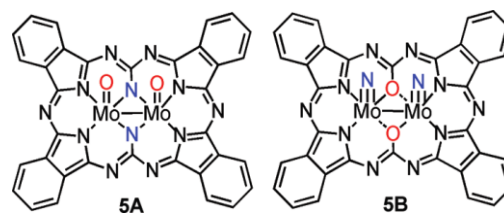


Fig. 5. Possible structures **5A** and **5B** based on the MS and ^1H NMR analyses
Рис. 5. Возможные структуры **5A** и **5B** на основе анализов ^1H ЯМР и МС анализов

The ^1H NMR data (Fig. 6) of **2** and **3** were also sufficient to support the X-ray crystallographic structures (Fig. 4). For example, the signals of **3** were assigned on the basis of both correlation spectroscopy (COSY) and nuclear Overhauser effect (NOE) experiments. Two α -benzo proton signals appear at 9.23 and 9.37 ppm as singlets with the same intensity, while *tert*-butyl proton signals were found at 1.42 and 1.51 ppm, indicating that **3** possesses a symmetry lower than the regular symmetry of D_{4h} metallo-Pcs.

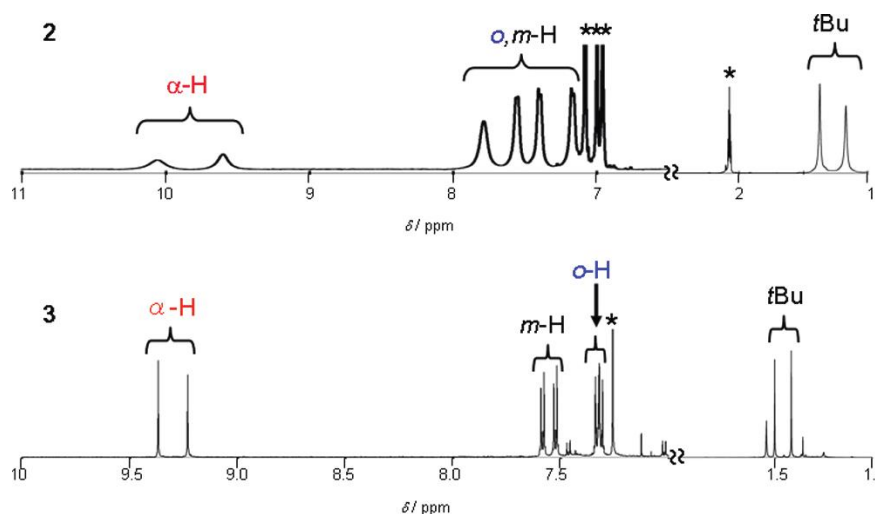


Fig. 6. ^1H NMR spectra of **2** in toluene- d_8 (top) and **3** in CDCl_3 (bottom). * Indicates residual solvent peaks
Рис. 6. Спектры ^1H ЯМР: **2** в толуоле- d_8 (вверху) и **3** в CDCl_3 (внизу). * Указывает на остаточные пики растворителя

On the other hand, the four doublets of the phenoxy protons observed in the 7.3–7.6 ppm region are similar to those at 7.1–7.3 ppm for 2,3,9,10,16,17,23,24-octa(*p-tert*-butyl)phenoxy zinc phthalocyanine (*t*-Bu-PhOZnPc). The fact that signals due to the α -benzo protons of **3** appeared significantly downfield relative to the corresponding protons of 4,5-di-*tert*-butylphenoxyphthalonitrile (7.82 ppm in CDCl_3) is consistent with the presence of a strong ring-current effect and a heteroaromatic π system. Similar trends as shown for **2** and **3** (Fig. 6) have been proposed for the ^1H NMR spectra of **1** and **4**.

When a Mo salt is used as a template in Pc syntheses in the presence of urea, nitride complexes of MoPc [(Mo V \equiv N)Pc] are known to be formed [20]. For the (Mo V \equiv N)Pcs reported to date, the IR signals associated with the Mo V \equiv N bond are observed in the 950–980 cm^{-1} range, while an intense electron paramagnetic resonance (EPR) signal due to the coupling of the unpaired electron with the five nitrogen atoms is observed at $g \approx 1.97$, along with weaker lines on each side due to electron–Mo 95 /Mo 97 coupling [21]. In this study, during the purification of **1a**, tetra-*tert*-butylated

(Mo^V≡N)Pc was obtained (HR-MS: *m/z* 871.2985 found for [M⁺+Na]; *m/z* 871.2984 calcd for C₄₈H₄₈MoN₉Na), and the anticipated IR band was observed at 974 cm⁻¹, while an EPR signal was detected at *g* = 1.977 in toluene at room temperature. When the IR spectrum of **1a** obtained from the same batch as the *tert*-butylated (Mo^V≡N)Pc was recorded, the spectrum shown in Fig. 7 was obtained. **1a** was found to be EPR-silent under the same conditions, which is reasonable considering the coordination geometry around the Mo ions and the presence of a Mo–Mo single bond as observed in the crystal structure of **2** (Fig. 4). Since the IR spectra of high-symmetry (*D*_{4h}) and low-symmetry Pc derivatives can be reliably reproduced by theoretical calculations in terms of both the energies and intensities of bands [22, 23, 28], calculated IR spectra were obtained for structures **5A** and **5B** (Fig. 5) and compared with the experimental data for compound **1a** (Fig. 7). A structure substituted with *tert*-butyl groups was optimized. Although the calculated spectra for **5A** and **5B** broadly reproduced the experimental data, we focused our attention on the 1080–970 cm⁻¹ region since **1a** displays three intense characteristic peaks at 1057, 1012, and 970 cm⁻¹. As is clearly shown in Fig. 7, these three strong peaks were reproduced when the Mo^V=O structure (**5A**) was used, while in contrast, when the Mo^V≡N structure (**5B**) was used only two intense peaks were predicted. Of the three intense peaks calculated for structure **5A**, the peak at the lowest energy (1014 cm⁻¹) corresponds to the peak observed at 970 cm⁻¹, which can be assigned as a Mo^V=O stretching vibrational mode. The Mo^V=O stretching vibrational modes of Pcs that have been reported previously have always appeared in the 970–975 cm⁻¹ region [25], while that of Mo^V≡N has been reported to lie between 950–980 cm⁻¹ [21]. These results therefore suggest that the compounds formed have a Mo^V=O structure (**5A**) [26].

The absorption, MCD, and fluorescence spectra of **2** are shown in Fig. 8, together with the absorption and MCD spectra of *tert*-butylated H₂Pc (*t*BuH₂Pc); the absorption and MCD spectra of **1**, **3**, and **4** can be compared in Fig. 9. The spectra of **1–4** are broadly similar and contain bands that can be readily assigned as the Q and B bands in the context of Gouterman's four-orbitals terminology [27]. The peak at longest wavelength is substantially red-shifted into the near-IR region relative to that of *t*BuH₂Pc, reflecting the expansion of the aromatic π systems of **1–4** relative to those of conventional Pcs.

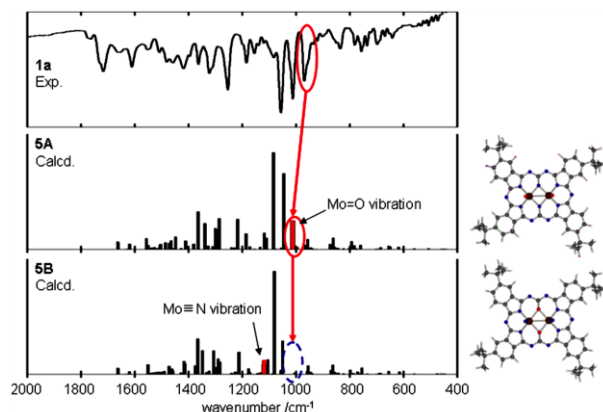


Fig. 7. Observed IR spectrum of **1a** (top) and theoretical IR spectra of structures **5A** (middle) and **5B** (bottom) with *tert*-butyl substituents. Marked bars indicate the vibrations involving Mo and its axial ligand
Рис. 7. Наблюдается ИК спектр **1a** (вверху) и теоретические ИК спектры структур **5A** (в центре) и **5B** (внизу) с *трет*-бутильными заместителями. Выделенные интервалы указывают на колебания, связанные с Mo и его осевым лигандом

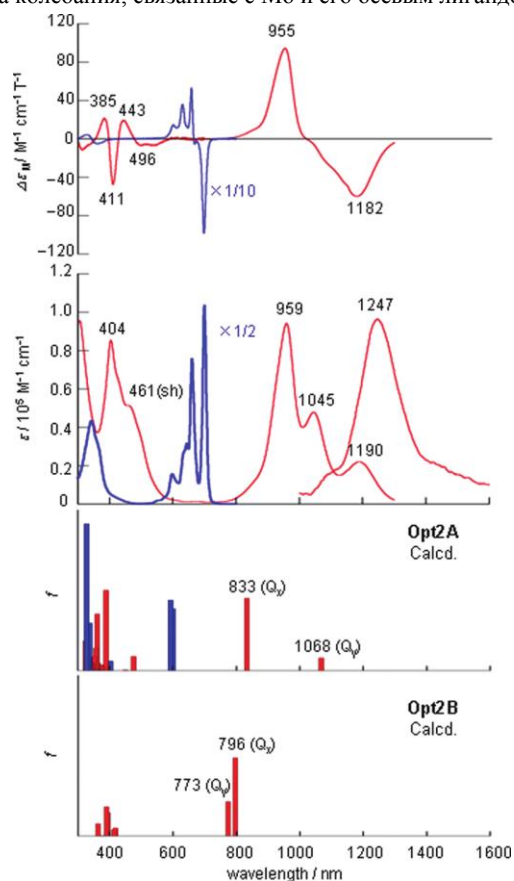


Fig. 8. Absorption (middle) and MCD (top) spectra of **2** (red) and *t*-BuH₂Pc (blue) in CHCl₃ and theoretical absorption spectra (bottom) of **Opt2A** and **Opt2B** (red) and H₂Pc (blue). The fluorescence spectrum of **2** in CHCl₃ is also shown in the middle panel (Fig. 8 in color see <http://journals.isuct.ru/ctj/article/view/1520>)

Рис. 8. Спектры поглощения (в центре) и MCD (вверху) для **2** (красный) и *t*-BuH₂Pc (синий) в CHCl₃ и теоретические спектры поглощения (внизу) **Opt2A** и **Opt2B** (красный) и H₂Pc (синий). Спектр флуоресценции **2** в CHCl₃ также показан на средней панели (Рис. 8 в цвете смотри <http://journals.isuct.ru/ctj/article/view/1520>)

The MCD spectra in the Q-band region are clearly dominated by Faraday B terms, since the intensity maxima and minima are closely aligned with the centers of the main absorption bands. This provides direct spectral evidence that the molecular symmetry of the compounds is lower than C_3 and that the excited states are nondegenerate, as would be anticipated on the basis of the C_{2v} symmetry of the crystal structure of **2**. The MCD bands observed in the 1000-1300 nm and 800-1000 nm regions can be assigned to symmetry-split y- and x-polarized Q_{00} bands, since coupled oppositely signed B terms would be anticipated in this context. Although three peaks are generally observed in the absorption spectra in Figs. 8 and 9, the second-lowest-energy band appears to be a vibrational component of the lowest-energy band, since the MCD signs are the same and the splittings between these bands are 1000-1200 cm^{-1} , which is typical of the spacing observed for vibrational bands in Pc spectra (ca. 1100 cm^{-1}) [28]. The optical spectra therefore provide strong evidence that compounds **1-4** arise from ring-expanded Pc analogues, which lack fourfold-symmetry axes.

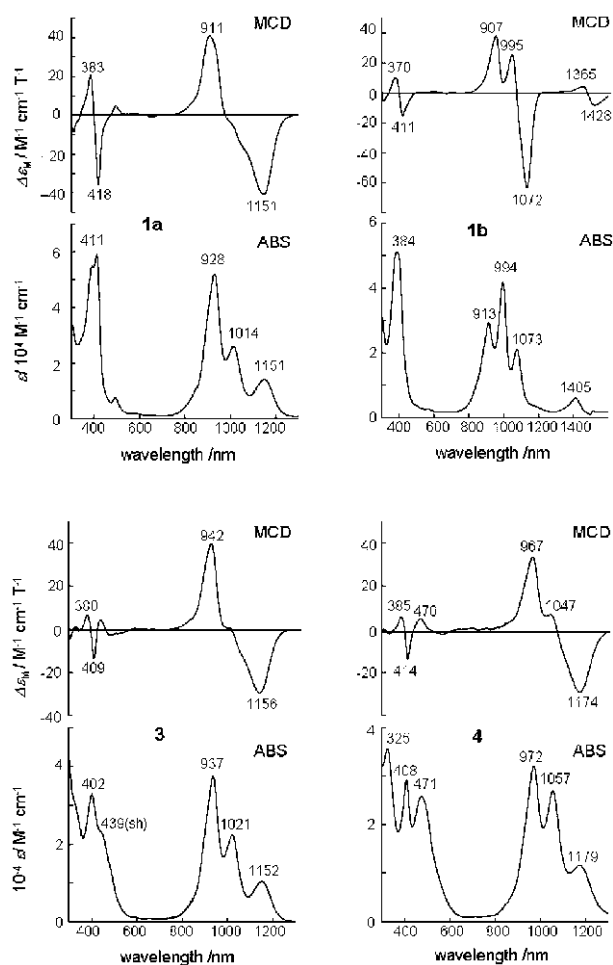


Fig. 9. Absorption (bottom) and MCD (top) spectra of **1a**, **1b**, **3**, and **4** in CCl_4

Рис. 9. Спектры поглощения (внизу) и MCD (вверху) **1a**, **1b**, **3** и **4** в CCl_4

The calculated absorption spectra based on structures containing $\text{Mo}^{\text{V}}=\text{O}$ (**5A**) and $\text{Mo}^{\text{V}}\equiv\text{N}$ (**5B**) are provided in the bottom portion of Fig. 8 (for details, see the next section). The closest match with the experimental spectrum was obtained using the Mo^{V} ion with an oxygen atom as the axial ligand. Compound **2** was found to have a weak emission peak at 1247 nm when excited at 404 nm (Fig. 8 middle).

Theoretical calculations were carried out to provide further insight into the electronic structures. Geometry optimization calculations were carried out using the structure of **5A** as a model compound. The optimized structure, **Opt2A**, is very similar to the crystal structure of **2**. In addition, the theoretical absorption spectrum (Fig. 8) and a molecular orbital (MO) diagram (Fig. 10) were calculated for **Opt2A** using TD-DFT (B3LYP/6-31G(d) for C, H, N, and O and LANL2DZ for Mo [29]) and compared with those of substituent-free H_2Pc .

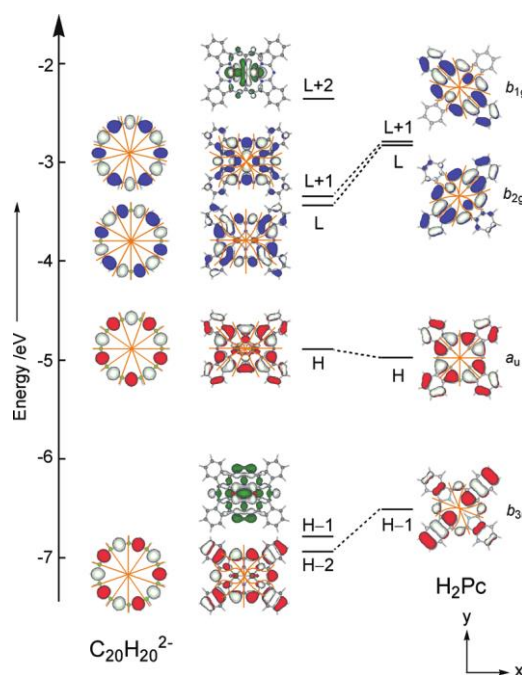


Fig. 10. MO diagrams of **Opt2A** and H_2Pc . H and L indicate the HOMO and LUMO, respectively. Arbitrary nodal lines have been drawn on the isosurface plots

Рис. 10. MO диаграммы **Opt2A** и H_2Pc . H и L обозначают HOMO и LUMO соответственно. На изоповерхностных участках проведены произвольные узловые линии

The symmetry-split Q bands of **Opt2A** were predicted to lie at 1068 and 833 nm, while those of H_2Pc were predicted to lie at 601 and 594 nm. The large splitting of the two bands (2642 cm^{-1}) and the much weaker intensity of the lower energy band of **Opt2A** ($f = 0.080$ compared with $f = 0.45$) are in close agreement

with the experimental data (splitting = 2025 cm⁻¹ and intensity ratio ≈ 1:5; Fig. 8). The Q bands were predicted to arise primarily from the four frontier π-MOs. The HOMO-1 was not included since it is derived mainly from *d* orbitals of the two Mo atoms. When **Opt2B**, which is based on the structure of **5B** with an Mo^V≡N core structure, was used instead, the Q bands were calculated to lie at 796 and 773 nm with a splitting of only 374 cm⁻¹, and the intensity ratio was the opposite of that observed experimentally. This provides further evidence that an Mo^V≡N core structure is unlikely to be present. In Fig. 10, the HOMO-LUMO gap of **Opt2A** is much smaller than that of H₂Pc. The marked red shift of the Q band of **2** relative to that of *t*BuH₂Pc is readily explained on this basis. The splitting of the LUMO and LUMO+1 is smaller than that of the HOMO and HOMO+1, as would be anticipated on the basis of the -/+ sign sequence observed for the Q bands in the MCD spectrum in ascending energy terms. Michl has demonstrated that a -/+ sign sequence is consistent with the orbital angular momentum properties that arise when the energy difference between the MOs derived from the HOMO of a parent hydrocarbon corresponding to the inner perimeter of the ligand (in this case the HOMO and HOMO-2) is larger than that between the MOs derived from the LUMO (in this case the LUMO and LUMO+1) [6, 30]. The number of nodes on the inner ligand perimeter of **Opt2A** frontier π-MOs is the same as the number observed for the frontier π-MOs of the C₂₀H₂₀²⁻ parent hydrocarbon perimeter. For example, five nodes are observed for the HOMO and HOMO-2 of **Opt2A** and the HOMO and HOMO-1 of C₂₀H₂₀²⁻. On this basis, it can be stated that the four frontier π-MOs of **Opt2A** are similar to those of a 20-atom, 22-π-electron annulene, which satisfies Hückel's (4n+2)π aromaticity rule. The strong intensity of the Q band in the MCD spectrum relative to that observed for the B-band region is related to the ΔM_L = ±11 change in orbital angular momentum properties that would be anticipated for the Q bands of **1-4** if the π systems were heteroaromatic [27]. The TD-DFT results therefore provide strong support for the conclusion that **Opt2A** and therefore **1-4** have a heteroaromatic 22-π-electron system.

Since the core structure was elucidated on the basis of the X-ray analysis of **2**, the aromaticity of this π system was evaluated by calculating nucleus-independent chemical shift (NICS) values. ¹H NMR chemical shifts were calculated for the corresponding non-substituted metal-free structures using DFT with the B3LYP functional and 6-31G(d) basis sets. The NICS values for expanded C_{2h} symmetric Pcs (i.e., the metal-free π structures of **1-4**) were calculated to be -11.8 ppm

at the center of the structure and -11.3 ppm at the center of the two central amino nitrogen and two pyrrole nitrogen atoms (i.e., the location of the Mo and W atoms in **1-4**), while a value of -13.5 ppm at the center of D_{2h}-symmetric nonsubstituted metal-free H₂Pc was predicted (Fig. 11). These values suggest that the expanded Pc has a ring-current effect similar to that of H₂Pc.

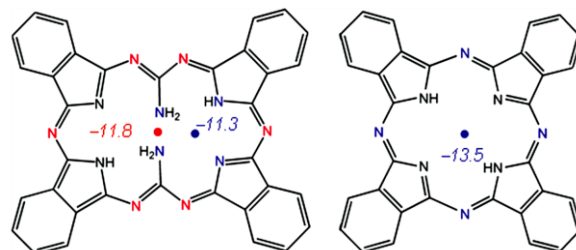


Fig. 11. NICS values of the expanded C_{2h}-symmetric Pc analogue and D_{2h}-symmetric free-base Pc. NICS values for the expanded Pc at the centers of the inner 20-membered ring and the central heteroatoms are shown in red and blue, respectively (Fig. 11 in color see <http://journals.isuct.ru/ctj/article/view/1520>)

Рис. 11. Значения NICS расширенного C_{2h}-симметричного аналога Pс и D_{2h}-симметричного свободного основания Pс. Значения NICS для расширенного Pс в центрах внутреннего 20-членного кольца и центральных гетероатомов показаны красным и синим соответственно (Рис. 11 в цвете смотри <http://journals.isuct.ru/ctj/article/view/1520>)

In summary, novel expanded phthalocyanine (Pc) congeners containing two Mo=O or W=O central cores and four isoindole moieties coordinated by four pyrrole nitrogen atoms and two amino nitrogen atoms have been synthesized under normal Pc formation conditions in the presence of urea. Their structures have been characterized using several spectroscopic methods, and their redox properties have been explored. X-ray analysis revealed a rectangular structure with C_{2v} symmetry. Although structures containing two Mo≡N or W≡N cores are also possible on the basis of the MS and ¹H NMR data, careful analysis of the X-ray, IR, and electronic absorption data and MO calculations has provided strong evidence for structures containing two Mo=O or W=O central cores. Electronic absorption bands in the 1200-1500 nm region were observed and could be readily assigned on the basis of Gouterman's four-orbital theory. Theoretical calculations were consistent with a heteroaromatic 22-π-electron system, which satisfies Hückel's (4n+2)π rule.

c) A Bottom-up Synthesis of Antiaromatic Expanded Phthalocyanines: Pentabenzotriazasmaragdyrins, i.e. Norcorroles of Superphthalocyanines [31]

Superphthalocyanine (SPc) is a only Pc analog containing five isoindole units., and has (4n+2) π type aromatic character. In 2015, the first examples of an antiaromatic expanded phthalocyanines, **3a** and **3b** (Scheme 5), classified as norcorroles of SPcs were prepared and fully characterized. The newly developed

phthalonitrile dimerization reaction was a crucial step, which allowed for the bottom-up synthesis of expanded phthalocyanines. Their structure was confirmed by single crystal X-ray diffraction analysis. The 20 π antiaromaticity of the macrocycles was suggested by optical and theoretical calculations.

The lithium method is a well-known synthetic protocol for free-base Pcs. The reaction is initiated by a nucleophilic attack of lithium alkoxide (oxyanion) on the cyano group of the phthalonitrile. The oxygen atom of the nucleophile is essential for the formation of Pcs. When carbanions are used as the nucleophile, tetra-benzotri-, di-, and monoazaporphyrins are obtained instead of Pcs [32]. These results motivated us to find alternative macrocyclic synthetic procedures using a different source of anion initiation. Thus, the thiolate anion, generated from dodecanethiol and sodium, was reacted with 4,5-disubstituted phthalonitrile (Scheme 5a). Although no macrocyclic compound was observed, an unexpected bright orange solid was obtained in moderate yields. Its structure, **2b**, was determined using single crystal X-ray diffraction analysis which revealed a diamino- β -isoindigo skeleton. Although the corresponding diimino- β -isoindigo skeleton has been reported by another group [33], this one-step synthesis of diamino- β -isoindigo skeleton has been explored for the first time. **2b** has a highly planar structure with two isoindole units in a transoid configuration.

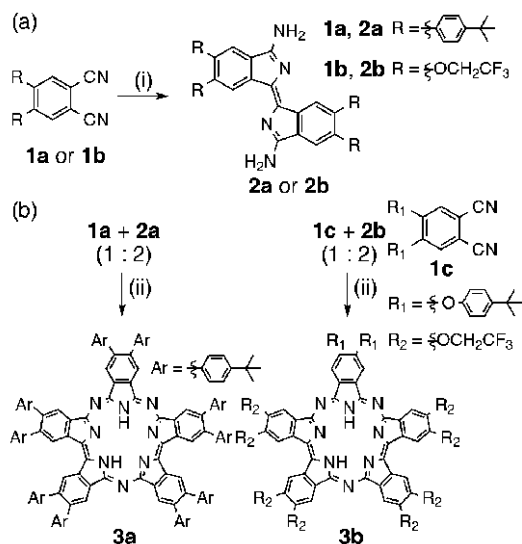


Схема 5. Синтез (а) диамино- β -изоиндиго и (б) пентабензотриазасмарагдиринов, **3a**, **3b**^а Реагенты и условия: (i) Na, 1-додекантиол, 100 °С, 1 ч, затем 180 °С, 1 ч, 50% (для **2a**), 39% (для **2b**); (ii) 1-хлорнафталин, 200 °С, 12 ч, 18% (для **3a**), 14% (для **3b**)

The condensation between phthalonitrile **1a** and aminoisoindigo **2a** at high temperatures produced the macrocyclic compound **3a** in an acceptable yield (Scheme 5b). In the case of different substituents between phthalonitrile (**1c**) and amino-isoindigo (**2b**), the 1:2 condensed macrocycle **3b** was obtained as the sole product. The ¹H NMR spectrum of **3a** showed five sets of signals arising from the α protons of isoindoles, reflecting a highly symmetric structure. More importantly, two sets of broad signals for inner NH protons appeared in the far low field region (20-24 ppm) for both **3a** and **3b**, owing to a strong paratropic ring current effect [34], indicating an antiaromatic character of compounds having **3**'s skeleton. The ¹H NMR spectra of **3a** and **3b** remained unchanged even after storage as a solid in air under ambient light for over 6 months.

The structure of **3** was unambiguously elucidated by X-ray diffraction analysis of crystals obtained from the diffusion of pyridine into an ethyl acetate solution of **3b** (Fig. 12).

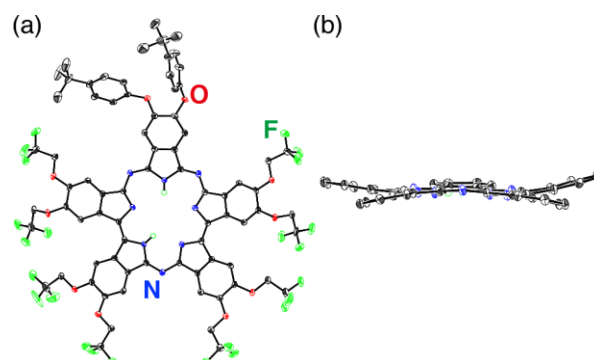


Fig. 12. X-ray crystal structure of **3b**. The thermal ellipsoids were scaled to the 50% probability level. (a) Top view; (b) side view (peripheral substituents were omitted)

Рис. 12. Рентгеновская кристаллическая структура **3b**. Тепловые эллипсоиды были масштабированы до уровня вероятности 50%. а) вид сверху; (б) вид сбоку (периферические заместители были опущены)

The macrocyclic skeleton of **3b** consists of five isoindole units with two direct pyrrole-pyrrole bonds. The whole structure is weakly twisted resulting from the steric interaction between the α protons of aminoisoindigo units. In contrast to 22 π aromatic smaragdyrins, the structure of **3b** can be interpreted as a 20 π electron macrocyclic delocalization pathway. Reflecting its (4n π) antiaromaticity in the solid state, compound **3b** displays significant bond length alternation (the HOMA index is 0.587). The NICS(0) and NICS(1) values calculated at the center of the macrocycle of model structure **3c**, where the peripheral substituents were replaced with hydrogen atoms, are 16.2 and 14.3 ppm, respectively, supporting the antiaromaticity of the macrocycle.

Absorption and MCD spectra of **3a** and **3b** are shown in Fig. 13. The absorption spectra exhibit significantly different envelopes from those of typical Pcs and superphthalocyanines [35].

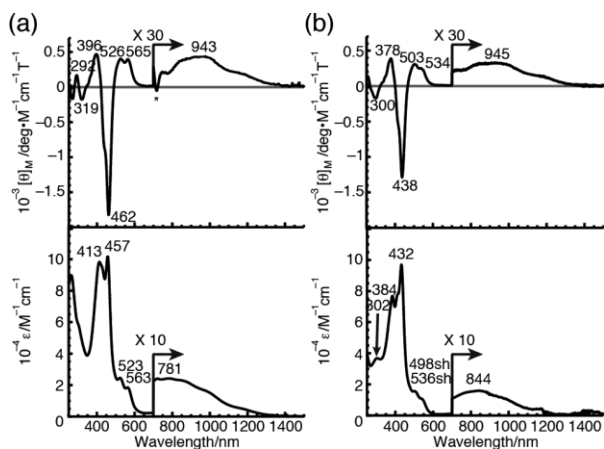


Fig. 13. UV-vis-NIR absorption (bottom) and MCD (top) spectra of (a) **3a** in CH_2Cl_2 and (b) **3b** in THF

Рис. 13. Спектры поглощения в УФ-видимой и ближней ИК-области (внизу) и МКД (вверху) для (a) **3a** в CH_2Cl_2 и (b) для **3b** в THF

Both compounds have weak and broad absorption bands ranging from 600 to 1300 nm, which are characteristic bands for $4n\pi$ antiaromatic porphyrinoids. Moderate (around 500 nm) and intense (around 400 nm) bands appeared in the visible region. In the MCD spectra, very weak and moderate Faraday B terms appeared, corresponding to the weak near-IR band and moderately intense band at around 500 nm, respectively. Strongly coupled Faraday B terms with a $-$, $+$ MCD sign in ascending energy were observed, corresponding to the absorption bands at around 400 nm.

To investigate further optical properties and the antiaromaticity of **3**, MO coefficients for modeled compound **3c** have been calculated. Partial MO energy diagrams and the calculated absorption spectrum of **3c** are shown in Fig. 14.

In our previous work, Michl's $4n$ -electron perimeter model [8-11] could be applied to the interpretation of absorption properties belonging to antiaromatic porphyrinoids [29, 36]. According to the model, six frontier π -orbitals of a 20-electron [18] annulene perimeter ($[\text{C}_{18}\text{H}_{18}]^{2-}$) are of particular importance for the 20π antiaromatic **3** and, thus, are also shown in Fig. 14. As can clearly be seen, the number of nodal planes (4, 5, and 6) of the six frontier orbitals belonging to **3c** are the same as those for $[\text{C}_{18}\text{H}_{18}]^{2-}$. The calculated lowest-energy band (1160 nm) is composed of transitions from the HOMO to the LUMO ($s_- \rightarrow s_+$). Since this transition is of an intrashell nature, the absorption

and MCD intensities of the band are very weak [10] and the observed weak near-IR band (781 nm for **3a**) could be assigned as the S band. Two weak (N_1 , N_2) and two strong (P_1 , P_2) transitions are also predicted on the basis of the perimeter model. The other four electronic transitions are intershell transitions derived from the (h_- or h_+) \rightarrow s_+ or $s_- \rightarrow$ (l_- or l_+) transition. Since the TD-DFT calculations of **3c** agree well with the antiaromatic perimeter model, the experimental absorption and MCD spectra could be assigned.

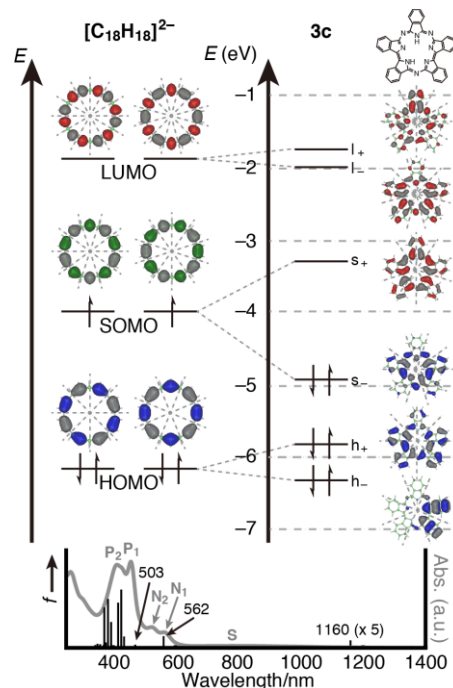


Fig. 14. Partial molecular energy diagram, orbitals, and perimeter labels of **3c** (top, right), its calculated absorption spectra (black sticks) and the absorption spectrum of **3a** in CH_2Cl_2 (gray line) (bottom), and 20-electron [18] annulene perimeter ($[\text{C}_{18}\text{H}_{18}]^{2-}$) (top, left)

Рис. 14. Диаграмма частичной молекулярной энергии, орбитали и метки периметра **3c** (вверху, справа), его рассчитанные спектры поглощения (черные палочки) и спектр поглощения **3a** в CH_2Cl_2 (серая линия) (внизу) и 20-электронном [18] периметре аннулена ($[\text{C}_{18}\text{H}_{18}]^{2-}$) (вверху слева)

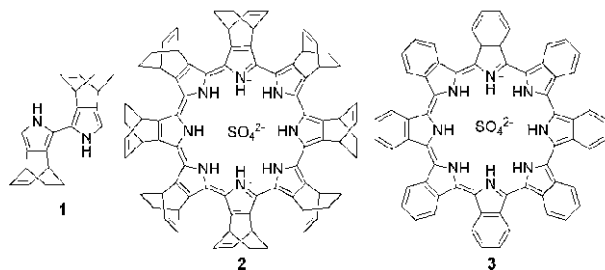
In summary, the first 20π expanded antiaromatic azaporphyrinoid (**3**) have been prepared and characterized. The sulfur-mediated phthalonitrile dimerization reaction was explored, allowing for the facile synthesis of diamino- β -isoindigos. Mixed condensation with aminoisoindigos and phthalonitriles produced new macrocyclic compounds consisting of five isoindole units. The crystal structure, ^1H NMR, absorption, and MCD spectra revealed clear 20π electronic conjugations both in solution and in the solid state. Moreover, Michl's $4n$ -electron perimeter model, in

conjunction with TD-DFT calculations, could be applied to explain the optical properties results. The new azaporphyrinoids were constructed using only phthalonitriles so that the expanded Pcs synthesis in this report is a true bottom-up synthesis that is led by new synthetic methodology.

2-5 Cyclo[*n*]pyrroles [37-39]

When the α -positions of *n* pyrrole molecules are connected to form cyclic compounds, the resultant molecules are called calix[*n*]pyrroles, and they are considered as porphyrin congeners in a broad sense. These molecules collected attention of particularly synthetic and spectroscopic chemists. We summarize here the synthesis and some spectroscopic properties developed and/or elucidated in our group.

The BCOD-fused 2,2'-bipyrrole **1** (Scheme 6) was prepared from BCOD-fused pyrrole according to literature procedures [37b]. All of the $\text{FeCl}_3 \cdot 6\text{H}_2\text{O}$ oxidant and H_2SO_4 were added to a 2 mM solution of **1** in CHCl_3 and stirred the mixture for 45 minutes at 0 °C. After purification by silica gel column chromatography and gel permeation chromatography (GPC), **2** was obtained as deep blue crystals in 43% yield. The MALDI-TOF mass spectrum contained a molecular ion peak at $m/z = 1241$ with eight daughter peaks with successive mass differences of $m/z = 28$, which is consistent with the presence of eight BCOD-fused pyrroles.



Scheme 6. Structures of bipyrrole **1** and octaphyrins **2** and **3**
Схема 6. Структуры бициррола **1** и октафиринов **2** и **3**

When **2** was heated as a solid at 240 °C in a glass tube under reduced pressure, the color changed from blue to yellow and cyclo[8]isoindole (**3**) was formed in almost quantitative yield. Crystals suitable for X-ray structure determination were obtained after recrystallization from $\text{CS}_2/\text{CHCl}_3$. The crystal structures of **2** and **3** are shown in Figs. 15 and 16.

In both cases, nonplanarity of the ligand and the geometry of the central SO_4^{2-} ion result in a D_{2d} molecular symmetry. The crystal structure of **2** is similar to that of the β -alkyl substituted cyclo[8]pyrroles reported by Sessler and co-workers[40] and contain a monoclinic cell, thus conforming to the $P_{21/c}$ space group with $Z = 4$. Alternating pyrrole moieties tilt

above and below the plane formed by the 16 α carbon atoms with a mean deviation of 0.1891 Å (Fig. 16). In contrast, a mean displacement of 0.4603 Å was reported for β -pyrrole-substituted cyclo[8]pyrroles [40]. This observation is consistent with our previous reports that fused BCOD moieties enhance the level of planarity of porphyrinoid π systems [41]. Dihedral angles of 20.8-27.88 are observed between adjacent pyrrole moieties, while the inner SO_4^{2-} ion is bound by six hydrogen-bonding interactions with $\text{NH} \cdots \text{O}$ distances ranging from 1.901 to 2.147 Å.

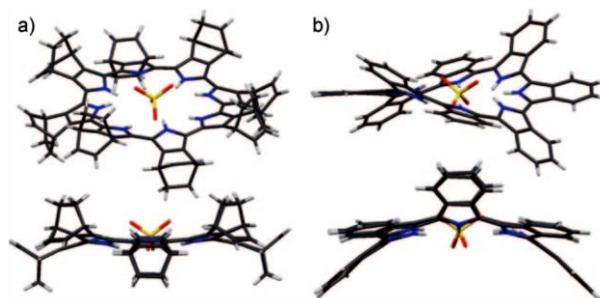


Fig. 15. Top and side views of the molecular structures of a) **2** and b) **3** with solvent molecules omitted for clarity

Рис. 15. Вид сверху и сбоку молекулярных структур а) **2** и б) **3** с молекулами растворителя, опущенными для ясности

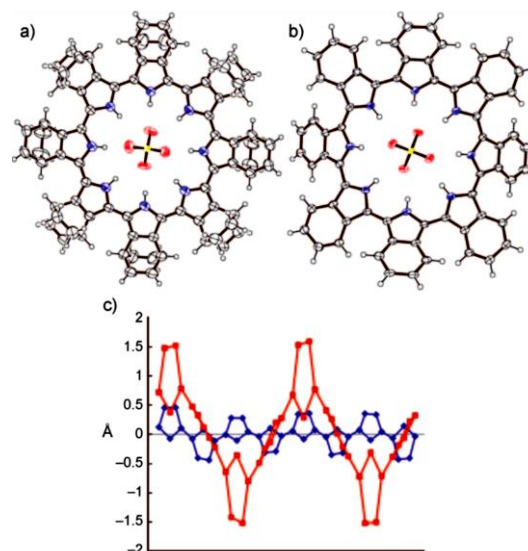


Fig. 16. ORTEP drawing of a) **2** and b) **3**. Solvent molecules are omitted for clarity. c) Deviation from the mean cyclo [8]pyrrole planes of **2** (blue) and **3** (red) (Fig. 16 in color see <http://journals.isuct.ru/ctj/article/view/1520>)

Рис. 16. Рисунок ORTEP для а) **2** и б) **3**. Молекулы растворителя для ясности опущены. в) Отклонение от средних цикло [8] пиррольных плоскостей **2** (синий) и **3** (красный) (Рис. 16 в цвете смотри <http://journals.isuct.ru/ctj/article/view/1520>)

Steric hindrance between the neighboring benzene rings of **3** at the ligand periphery results in a deeper saddling distortion of the cyclo[8]isoindole π system (Figs. 15 and 16), which crystallizes in a monoclinic cell that conforms to space group $P2_1/c$. The

mean deviation from the cyclo[8]pyrrole plane is 0.6081 Å, more than three times higher than the value for **2**. The dihedral angles between adjacent pyrroles of 20.5–29.08° are similar, however. There is a slight bending of the isoindole moieties with dihedral angles of 1.98–2.078° between the pyrrole and fused benzene moieties (Fig. 15).

As for the above **2** and **3**, acenaphthylene-fused cyclo[8]pyrrole **5** and cyclo[10]pyrrole **6** were prepared using 2,2',5,5'-tetra-*tert*-butyl-7,7'-bicenaphtho[1,2-*c*]pyrrole **4** in ca. 20–40 and 45–70% yield, respectively under the best conditions (Figs. 17 and 18).

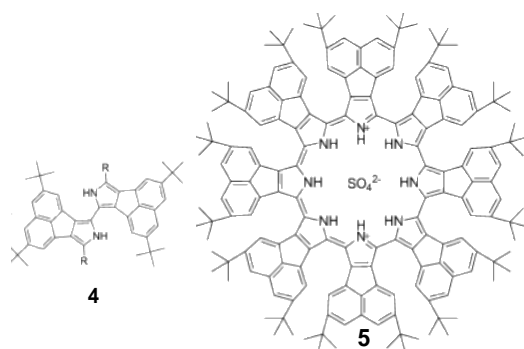


Fig. 17. Structures of **4** and acenaphthylene-fused cyclo[8]pyrrole **5**
Рис. 17. Структура **4** и аценафтилен-конденсированного цикло[8] пиррола **5**

In the case of **5**, $\text{Ce}(\text{SO}_4)_2$ and H_2SO_4 were used as oxidant and acid respectively, and $\text{Na}_2(\text{SO}_4)$ and $\text{N}(\text{Bu})_4\text{HSO}_4$ were used as additives. For **6**, croconic acid and FeCl_3 were used as a template and oxidant, respectively. Without croconic acid, **6** was not formed.

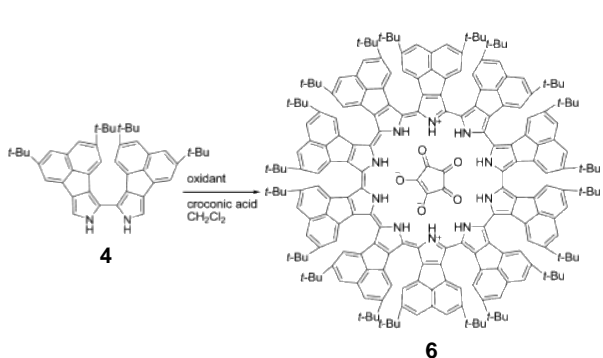


Fig. 18. Structures of **4** and acenaphthylene-fused cyclo[10]pyrrole **6**
Рис. 18. Структура **4** и аценафтилен-конденсированного цикло[10] пиррола **6**

Crystals of **5** were obtained in two forms (*a* and *b*) shown in Fig. 19. Isomer **5a** crystallized in a triclinic unit cell (space group $P1\bar{1}$, $Z = 2$). Although relatively weak reflections were observed, the structure

of the less-polar **5b** isomer was successfully solved and refined (Fig. 19b). A similar structure was elucidated by means of X-ray diffraction studies with a synchrotron radiation X-ray beam. When only the cyclo[8]pyrrole ligand is considered, **5a** has an S_8 rotoinversion axis, whereas **5b** has C_s symmetry. In the structure of **5a**, alternating pyrrole moieties tilt above and below the mean plane. Dihedral angles of 11.2–19.8 and 23.9–31.0° are observed between the mean plane and pyrrole moieties and between adjacent pyrrole moieties, respectively, whereas the inner SO_4^{2-} ion is bound by six hydrogen-bonding interactions with $\text{NH}\cdots\text{O}$ distances of 1.907–2.264 Å. In contrast, the less-polar **5b** structure adopts a conformation in which the pyrrole moiety (labeled D in Fig. 19c) flips in orientation from that observed in the alternating tilting structure of **5a**. Dihedral angles of 28.0–37.2° are observed between the mean plane and pyrroles B, D, and F (see Fig. 19c). In contrast, the dihedral angles of 24.4–34.7° between adjacent pyrroles are similar to those in the structure of **5a**. There is a slight bending of the acenaphthopyrrole moieties with dihedral angles of 11.6–20.4 and 8.8–22.1° between the pyrrole and acenaphthylene rings for **5a** and **5b**, respectively.

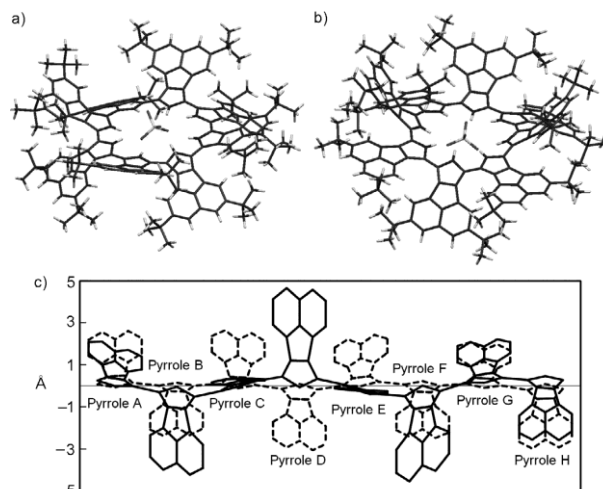


Fig. 19. Molecular structures of a) **5a** and b) **5b**. c) Deviation from the mean cyclo[8]pyrrole planes of **5a** and **5b** (dotted and solid lines, respectively). The disordered atoms of the peripheral *tert*-butyl substituents are omitted for clarity

Рис. 19. Структура молекул а) **5a** и б) **5b**. в) Отклонение от средних цикло[8] пиррольных плоскостей **5a** и **5b** (пунктирные и сплошные линии соответственно). Разупорядоченные атомы периферических *т*ерц-бутильных заместителей для ясности опущены

A single crystal of **6** was obtained after recrystallization from chlorobenzene/*n*-heptane and was used for X-ray crystallographic analysis. The crystal structures are shown in Fig. 20. Compound **6** crystallized in

a triclinic unit cell (space group $P1, \bar{Z} = 2$). Alternating pyrrole moieties tilt above and below the mean plane. The inner croconate anion is bound by ten hydrogen-bonding interactions with $\text{NH} \cdots \text{O}$ distances of 1.784–2.015 Å, which are slightly shorter than the distances between the SO_4^{2-} anion and the pyrrolic NH of cyclo[8]pyrroles since the croconate anion adopts the planar structure. Thus, croconate anion acts as a template for cyclization because its size fits with the central space of the pyrrolic macrocycle. Dihedral angles of 14.1–18.0° and 30.4–32.9° are observed between the mean plane and pyrrole moieties and between adjacent pyrrole moieties, respectively, which are similar to those of the symmetrical conformational isomer of cyclo[8]acenaphthopyrrole (**5a** in Fig. 19c).

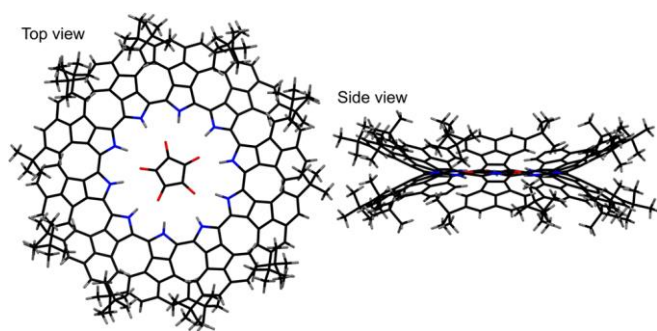


Fig. 20. Molecular structure of cyclo[10]acenaphthopyrrole **6**. Disordered (less popular) atoms and solvents are omitted for clarity
Рис. 20. Структура молекулы цикло [10] аценафтопиррола **6**. Неупорядоченные (менее популярные) атомы и растворители для ясности опущены

Fig. 21 shows the experimental spectra for **2**, **3** and **5a**, with the TD-DFT spectra calculated for the B3LYP-optimized geometries plotted against a secondary axis. An intense band is observed in the spectrum of **5a** in the near-IR region at 1482 nm, while there is a weaker band in the visible region at 512 nm. The spectroscopic shape is broadly similar to each other, but the major bands are shifted significantly to the red with increasing the π system. Also, the relative intensities of the major spectral bands in the near-IR and visible regions differ markedly.

The electronic absorption and MCD spectra of **6** are shown in Fig. 22, together with its calculated absorption spectrum. The L band appeared at 1982 nm compared with 1481 nm for **5**. Thus, the expansion of two acenaphthopyrroles has resulted in markedly redshift of the L band by ca. 500 nm (ca. 1710 cm^{-1}). In the UV–visible region, absorption peaks are observed at 549, 428, and 365 nm. In the MCD, negative A-term-like curves were observed corresponding to most of the absorption peaks, with an apparent L band intensity about 20 times larger than that of the other bands. From

the sharp dispersion-type MCD curve and the results of molecular orbital calculations described later, the band at 428 nm appears to be the B band. These optical properties can be understood with reference to a $\text{C}_{30}\text{H}_{30}^{8-}$ parent hydrocarbon that corresponds to the inner ligand perimeter with MOs arranged in an $M_L = 0, \pm 1, \pm 2, \dots, \pm 13, \pm 14, 15$ sequence in ascending energy. An allowed B band and a forbidden L band are related to $\Delta M_L = \pm 1$ (transitions from $M_L = -9$ to -10 and $M_L = +9$ to $+10$ MOs) and $\Delta M_L = \pm 19$ (transitions from $M_L = -9$ to $+10$ and $M_L = +9$ to -10 MOs) properties, respectively. Since the MCD intensity mechanism is based on the relative magnitude of the magnetic moments of the $\pi\pi^*$ excited states, the intensity of the L MCD band with “ $\Delta M_L = \pm 19$ ” property is much (around 20 times) stronger than that of the B band with $\Delta M_L = \pm 1$, as is observed experimentally (Fig. 22).

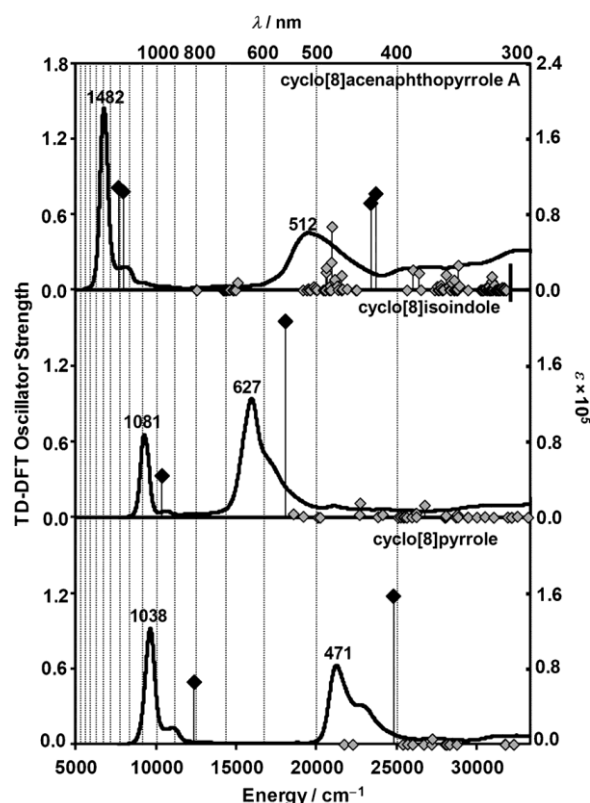


Fig. 21. The calculated TD-DFT spectra for the B3LYP-optimized structures of the cyclo[8]pyrrole, cyclo[8]isoindole, and cyclo[8]acenaphthopyrrole model complexes. Experimental spectra for a BCOD-fused cyclo[8]pyrrole **2**, benzo-fused **3**, and acenaphtho-fused **5a** are plotted against a secondary axis. Black diamonds highlight the L and B bands

Рис. 21. Рассчитаны спектры TD-DFT для B3LYP-оптимизированных структур модельных комплексов цикло [8] пиррола, цикло [8] изоиндола и цикло [8] аценафтопиррола. Экспериментальные спектры для BCOD-конденсированного цикло [8] пиррола **2**, бензо-конденсированного **3** и аценафто-конденсированного **5a** построены на вторичной оси. Черные ромбы подчеркивают полосы L и B

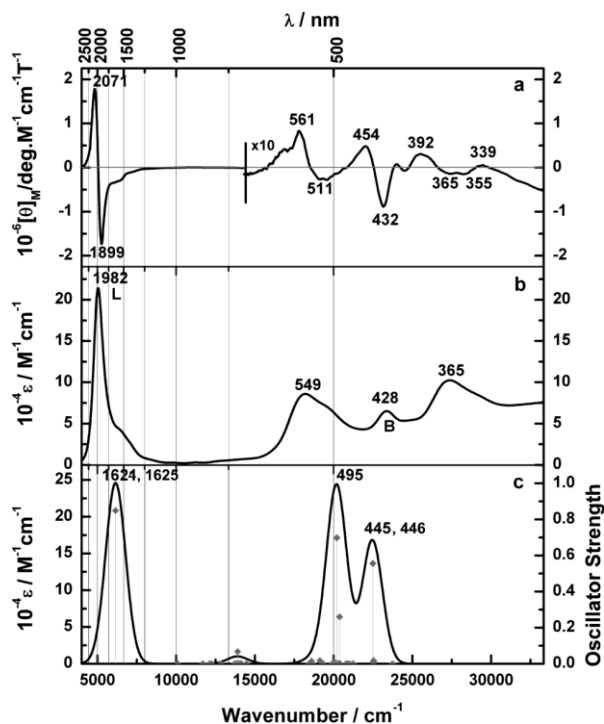


Fig. 22. Experimental (a) MCD and (b) UV-vis-NIR and (c) calculated UV-vis-NIR spectra of cyclo[10]-acenaphthopyrrole **6** using the B3LYP/SDD level

Рис. 22. Экспериментальные (а) MCD и (b) UV-vis-NIR и (с) вычисленные UV-vis-NIR спектры цикло [10]-аценафтопи-рола **6** с использованием уровня B3LYP / SDD

Fig. 23 shows the MO energies and some MOs in TD-DFT calculations based on the B3LYP-optimized geometry of **6**, which is close to its X-ray structure. In compound **6**, some degenerate orbitals in a high-symmetry parent hydrocarbon perimeter are raised, due to a structural perturbation. When the C_{30} axis of $C_{30}H_{30}^{8-}$ is replaced by an S_5 in the proper rotation axis in the context of D_{5d} symmetry with respect to **6**, only the degeneracy of MOs with $M_L = \text{odd}$ number is retained, while that of those with $M_L = \text{even}$ number are split.

This outcome means that the HOMOs ($M_L = \pm 9$) are degenerate in **6**, while the LUMOs ($M_L = \pm 10$) are split, in contrast to normal D_{4h} type porphyrinoids, in which the HOMOs with $M_L = \pm 4$ are symmetry-split, while the LUMOs with $M_L = \pm 5$ are degenerate [27]. In understanding the MCD spectra of chromophores, the degeneracy in the ground and/or excited states and the relative energy splitting of the HOMO and HOMO-1 ($\Delta HOMO$) and LUMO+1 (in this study LUMO+12) and LUMO ($\Delta LUMO$) are important. When the excited state is orbitally degenerate, as in this case, a derivative-shaped MCD curve (called A-term) is observed, associated with an absorption peak, and its signal

changes from plus-to-minus if $\Delta LUMO > \Delta HOMO$ is in ascending energy [12, 42, 13, 6, 7]. Conversely, a minus-to-plus MCD pattern appears if $\Delta LUMO < \Delta HOMO$, as is generally seen for normal porphyrinoids. In accordance with these MCD characteristics, **6** showed a plus-to-minus MCD sequence corresponding to both the L and B bands.

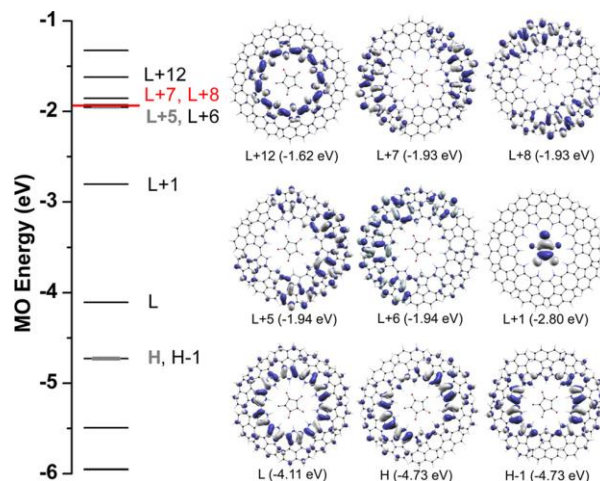


Fig. 23. Partial molecular energy diagram and some orbitals contributing to absorption spectrum for the B3LYP-optimized geometries of **6**. Note that L+1 is not ligand-centered

Рис. 23. Диаграмма частичной молекулярной энергии и некоторые орбитали, вносящие вклад в спектр поглощения для геометрий, оптимизированных B3LYP для **6**. Обратите внимание, что L + 1 не является лиганд-центрированной

The calculated absorption spectrum in Fig. 22c broadly reproduces the experimental data. The L and B bands were calculated at 1625 (and 1624) and 446 (and 445) nm, and from the configuration (not shown), the band estimated at 495 nm corresponds to transitions from the HOMO-1 to the fused acenaphthylene-centered orbitals (LUMO+2 to LUMO+11). The emergence of a red-shifted, intensified L band (HOMO, HOMO-1 to LUMO transition) may be explained using the results in Fig. 23 together with Michl's perimeter model [6, 7]. When aromatics such as acenaphthylene or benzene are added to the pyrrole rings of cyclo[10]pyrrole, whether the ring annulation results in a stabilization or a destabilization is related to the presence and absence, respectively, of nodal planes through the ten pyrrole N atoms and the peripheral fused aromatics. Thus, compared with a LUMO, which has bonding interaction with the annulated aromatics, the LUMO+12 with ten nodal planes and having anti-bonding interaction with the annulated ring is greatly destabilized (Fig. 24), resulting in an increase in the (LUMO+12 – LUMO) value (Fig. 23), and a further

decrease of the (HOMO–LUMO) value, i.e., a red-shift of the L band. Conversely, in the case of normal porphyrinoids such as tetrabenzoporphyrin (TBP), an antibonding interaction occurs for MOs having nodal planes through the four pyrrole N atoms (Fig. 24), producing an increase in the (HOMO–HOMO-1) value. As nicely explained by Gouterman's 4-orbital model [27], the Q-band gains intensity, as the energy difference between the HOMO and HOMO-1 increases. In a similar manner, a large energy difference between the LUMO+12 and LUMO (Fig. 23) produces the intensified L band here.

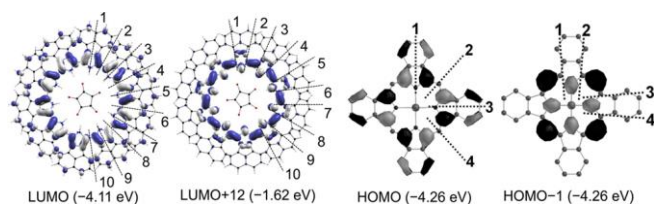


Fig. 24. Nodal patterns of the LUMO and LUMO + 12 of **6** (left) and the HOMO and HOMO - 1 of TBP (right) at an isosurface value of 0.025 atomic units (hartrees) with the $M_L = \pm 10$ and ± 4 nodal plane properties highlighted

Рис. 24. Узловые структуры LUMO и LUMO + 12 для **6** (слева) и HOMO и HOMO - 1 TBP (справа) при значении изосurface 0,025 атомных единиц (хартри) с выделенными свойствами узловой плоскости $M_L = \pm 10$ и ± 4

In summary, we have succeeded in preparing cyclo[8/10]pyrroles with varying π -conjugation systems. With the increase of the π -system, both the L and B bands shifted to longer wavelengths. In the case of the acenaphthylene-fused cyclo[10]pyrrole complex **6**, not only the assignment of the bands, but also the intensity and sign of the MCD spectra were illustrated and reasonably explained. Different from normal porphyrins, cyclo[8/10]pyrroles introduced here have degenerate HOMOs and the LUMOs degeneracy is lifted.

2-6 $4n\pi$ and $(4n+3)\pi$ Systems

a) Application of the Perimeter Model to the Assignment of the Electronic Absorption Spectra of Gold(III) Hexaphyrins with $[4n+2]$ and $[4n]$ π -Electron Systems [43]

We prepared Au complexes of hexaphyrin shown in Fig. 25. When the compounds in the left-hand side (**Au₂-N** and **Au-N**) are reduced by NaBH₄, two imino nitrogens in the central moiety are reduced and the compounds in the right-hand side (**Au₂-R** and **Au-R**) were obtained. The absorption spectra of **Au₂-N** and **Au-N** (not shown) are those of normal $[4n+2]$ type, showing weak Q and strong Soret bands.

However, the absorption and MCD spectra of **Au₂-R** and **Au-R** (Fig. 26) were quite different from those of normal porphyrins, and finally found to be those of typical $4n\pi$ cyclic compounds as follows.

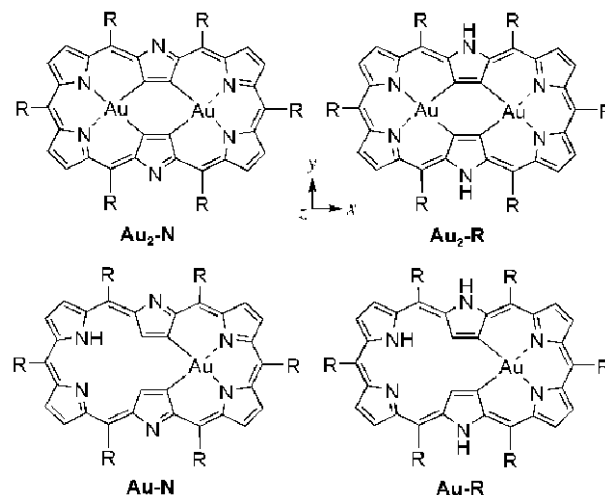


Fig. 25. Hexaphyrin Au complexes in the neutral (left) and reduced (right) forms

Рис. 25. Комплексы гексапиррина Au в нейтральной (слева) и восстановленной (справа) формах

Fig. 26 shows the MCD and electronic absorption spectra of the reduced forms of the hexaphyrins (**Au₂-R** and **Au-R**). The reduced forms do not exhibit the remarkable NIR absorption bands observed in the neutral forms. However, when we carefully measured the absorption spectra, a weak, structureless absorption band was detected in the NIR region. In the visible region, intense absorption bands observed for the neutral hexaphyrins shifted to the blue. It is noteworthy to mention that two distinct absorption shoulders are seen in the 600-700 nm region for both complexes. When the spectra of these complexes were measured in toluene and methanol, the spectral patterns remained virtually unchanged. We measured the MCD spectra of these complexes in the UV-visible-NIR region. Strongly coupled Faraday B terms with +, - MCD sign in ascending energy were observed, corresponding to the absorption bands at 539 and 570 nm for **Au₂-R**. Similar coupled MCD signals are seen for the 497 and 569 nm absorption bands of **Au-R**, but their MCD intensities are somewhat weaker than those observed for **Au₂-R**. This may result from the energy separation of two electronic excited states, since the intensity of coupled B terms is inversely proportional to the energy difference between two states [12, 13, 6, 7]. Weak MCD signals were observed for the two absorption shoulders

at longer wavelength to the intense bands of both complexes. No MCD signals were observed in the NIR region.

The calculated stick spectra of the reduced form of the hexaphyrins without a C_6F_5 group (Au_2-R' , $Au-R'$) are presented at the bottom of Fig. 26, with the calculation results summarized in Table. The calculated spectral features appear to be in reasonable agreement with the observed spectra. The reduced species are predicted to have two blue-shifted absorption bands compared with the neutral species. The 445 nm transition calculated for Au_2-R' is polarized along the x axis, while the polarization of the 509 nm band is the y axis. Since the mutually perpendicular transitions have coupled Faraday B terms, the observed 539 and 590 nm absorption bands are attributed to these transitions. The third absorption band (508 nm) is considered to be a vibronic band of the 539 nm absorption band. The excitation wavelengths of the mono-gold complex are almost identical to those of the bis-gold complex, reproducing well the experimental spectra. Two very weak electronic transitions are calculated at around 600-670 nm for Au_2-R' and $Au-R'$, which can be correlated with the observed absorption shoulders. Interestingly, four low-energy electronic transitions consist mainly of electronic transitions involving the six frontier π orbitals, which can be labeled as h_- , h_+ , s_- , s_+ , l_- , and l_+ by applying the perimeter model (details are discussed in the following section). The TDDFT calculations also predict that the forbidden HOMO \rightarrow LUMO ($s_- \rightarrow s_+$) transition is located beyond 2000 nm for both complexes. Although the present calculations underestimate the excitation energies, the weak NIR absorption band observed is assigned to the HOMO \rightarrow LUMO ($s_- \rightarrow s_+$) transition. This type of forbidden transition is characteristic of unaromatic cyclic π -electron systems [8-11].

According to the 4N-electron perimeter model, six frontier π -orbitals are of particular importance [8-11]. These orbitals are derived from the highest doubly occupied (HO), the singly occupied (SO), and the lowest unoccupied (LU) doubly degenerate orbitals of an ideal 4N-electron perimeter. Fig. 27 shows the six frontier molecular orbitals of a 28-electron [24]annulene perimeter ($[C_{24}H_{24}]^{4+}$) and Au_2-R' . As is clearly seen in the Figure, the number of nodal planes of the six orbitals of Au_2-R' is the same as that of $[C_{24}H_{24}]^{4+}$. Essentially identical nodal properties were calculated for the mono-gold complex ($Au-R'$).

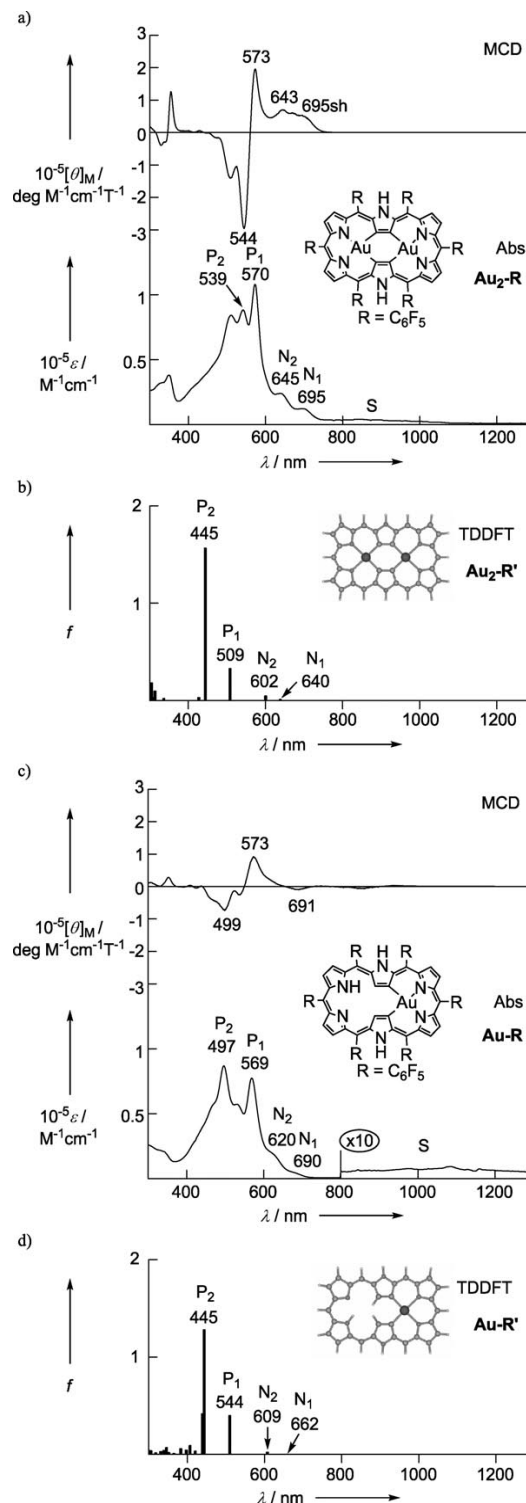


Fig. 26. MCD and absorption spectra of the reduced forms of hexaphyrins recorded in CH_2Cl_2 at room temperature (a: Au_2-R , c: $Au-R$). The calculated stick absorption spectra (B3LYP/LanL2DZ) of the hexaphyrins without peripheral substituents are shown in b) Au_2-R' and d) $Au-R'$. The inset shows the optimized structures of Au_2-R' and $Au-R'$ (B3LYP/LanL2DZ).
Рис. 26. MCD и спектры поглощения восстановленных форм гексаферинов, записанные в CH_2Cl_2 при комнатной температуре (a: Au_2-R , c: $Au-R$). Рассчитанные спектры поглощения (B3LYP/LanL2DZ) гексаферинов без периферических заместителей показаны для b) Au_2-R' и d) $Au-R'$. На вставке показаны оптимизированные структуры Au_2-R' и $Au-R'$ (B3LYP/LanL2DZ).

TDDFT results for low-energy π - π^* states of unaromatic hexaphyrins (B3LYP/LanL2DZ)Таблица. Результаты TDDFT для низкоэнергетических π - π^* состояний неароматических гексафиров (B3LYP / LanL2DZ)

	Assign. ^[a]	Sym	λ /nm	Pol	f	Contribution (weight %) ^[b]
Au₂-R'	S	A ₁	2069	-	0.0000	s ₋ →s ₊ (88.0)
	N ₁	B ₂	640	y	0.0117	h ₊ →s ₊ (55.0), s ₋ →l ₋ (45.8)
	N ₂	B ₁	602	x	0.0471	h ₋ →s ₊ (58.1), s ₋ →l ₊ (41.8)
	P ₁	B ₂	509	y	0.3276	s ₋ →l ₋ (40.0), h ₊ →s ₊ (26.7)
	P ₂	B ₁	445	x	1.5660	s ₋ →l ₊ (44.2), h ₋ →s ₊ (22.3)
Au-R'	S	A	2137	-	0.0001	s ₋ →s ₊ (86.5)
	N ₁	A	662	-	0.0036	s ₋ →l ₋ (57.4), h ₊ →s ₊ (36.8)
	N ₂	A	609	-	0.0218	s ₋ →l ₊ (43.5), h ₋ →s ₊ (40.9)
	P ₁	A	511	y	0.3979	h ₊ →s ₊ (26.8), s ₋ →l ₋ (23.3), h ₋ →l ₋ (11.8)
	P ₂	A	445	x	1.2781	s ₋ →l ₊ (27.8), h ₋ →s ₊ (20.0), h ₋ →s ₊ (15.7)

[a] Perimeter state label. [b] s₋ = HOMO, s₊ = LUMO.

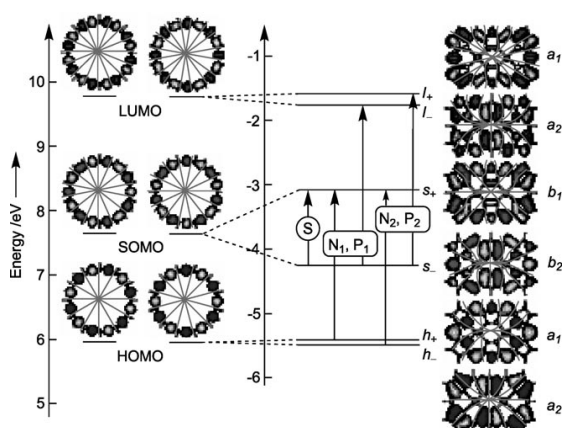


Fig. 27. Iso-surface plots of the frontier MOs, energy levels, and perimeter labels of 28-electron [24]annulene perimeter ($[C_{24}H_{24}]^{4+}$) and **Au₂-R'** (B3LYP/LanL2DZ). Arbitrary nodal lines are drawn on the iso-surface plots. HOMO = s₋, LUMO = s₊

Рис. 27. Графики изоповерхности пограничных МО, энергетических уровней и меток периметра периметра с 28 электронами [24] аннулена ($[C_{24}H_{24}]^{4+}$) и **Au₂-R'** (B3LYP / LanL2DZ).

На изоповерхностных участках изображены произвольные узловые линии. HOMO = s₋, LUMO = s₊

The frontier orbitals of **Au₂-R'** and **Au-R'** can therefore be derived from the perimeter orbitals, and the HOMO-2, HOMO-1, HOMO, LUMO, LUMO+1, and LUMO+2 are labeled as h₋, h₊, s₋, s₊, l₋, and l₊, respectively. The origin of the peculiar spectral features of the reduced forms will now be discussed using the model. The five singly excited states considered in the perimeter model, S, N₁, N₂, P₁, and P₂, arise as shown in Fig. 27. As we described in the previous section, the lowest-energy transition is the s₋→s₊ transition. Since the transition is of an intrashell nature in the perimeter model, the transition is magnetic-dipole allowed, but the absorption and MCD intensities are predicted to be zero [8-11]. Indeed, the observed absorption and MCD intensities of the S band are very weak. The other four electronic transitions are intershell transitions derived

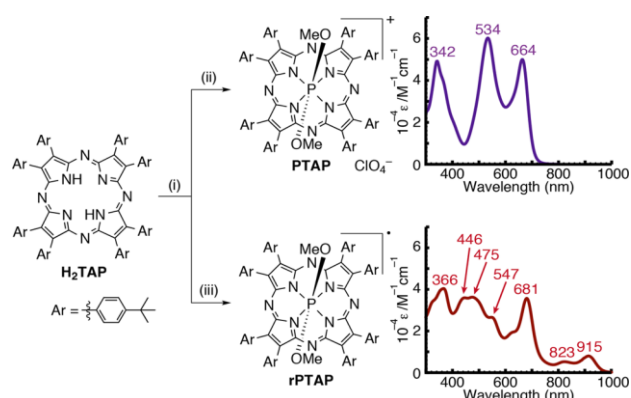
from the HO→SO or SO→LU transition. Two weakly (N₁, N₂) and two strongly (P₁, P₂) electric-dipole allowed transitions are predicted on the basis of the perimeter model. The N and P transitions can be related to the L and B transitions of aromatic systems. Thus, a significant mixing of the h₊→s₊ and s₋→l₋ transitions causes cancellation and intensification of the transition dipole moments in the N₁ and P₁ bands, while weak N₂ and intense P₂ bands are due to a significant mixing of the h₋→s₊ and s₋→l₊ transitions. The present TDDFT calculations of **Au₂-R'** and **Au-R'** agree well with the perimeter model and we can assign the experimental absorption spectra by using the perimeter model and computational results: the weak absorption bands observed at 695 and 645 nm for **Au₂-R** are N₁ and N₂ bands, while the intense 590 and 539 nm bands are P₁ and P₂ bands, respectively. Similar band assignments can be made for **Au-R**.

Finally, the observed MCD sign pattern of the reduced forms is discussed. Strongly coupled Faraday B terms with a +,- pattern in ascending energy were observed for the two P bands of both complexes. Since the electric transition dipole moments for the P bands are much larger than those for N bands, the sign of the coupled B terms are likely to be dominated by contribution from magnetic mixing within the two P states. As shown in Table, the transition from the ground state to the P₁ state consists of the s₋→l₊ and h₊→s₊ transitions, while that to the P₂ state consists of the s₋→l₋ and h₋→s₊ transitions. According to the perimeter model, coupling between s₋→l₋ and s₋→l₊ transitions gives rise to a -, + pattern for the two P bands, while coupling between h₊→s₊ and h₋→s₊ transitions causes a +, - pattern [8-11]. Since a +,- pattern is observed, the coupling between the h₊→s₊ and h₋→s₊ transitions must be dominant for the MCD signals of the present hexaphyrins. Thus, the 4N-electron perimeter model was

successfully used for the analysis of the reduced form of Au hexaphyrins.

b) An Extremely Air-Stable 19π $\{(4n+3)\pi\}$ Porphyrinoid [44]

We observed during our experiments, that the color of the crude solution of the octa(*p*-*tert*-butylphenyl) TAP phosphorus(V) complex (**PTAP**) changed from purple to brown on adding triethylamine. The polarity of this brown species was much lower than that of the original cationic species, and we were able to isolate the brown species (**rPTAP**) as a stable solid by conventional Al_2O_3 open column chromatography with a basic eluent (CH_2Cl_2 -triethylamine) (Scheme 7).



Scheme 7. Synthesis of cationic (**PTAP**) and neutral (**rPTAP**) states of the tetraazaporphyrin (TAP) phosphorus(V) complex and their absorption spectra in CH_2Cl_2

Схема 7. Синтез катионных (**PTAP**) и нейтральных (**rPTAP**) состояний комплекса тетраазпорфирина (TAP) фосфора (V) и их спектры поглощения в CH_2Cl_2

Peripheral *p*-*tert*-butylphenyl groups were suitable for isolation of the reduced species. The absorption properties of **rPTAP** are quite different from those of **PTAP**. The sharp absorption band at around 660 nm is retained (at 681 nm), while bands around 500 nm are broad and weak, and near-IR bands (915 and 823 nm) appear only for **rPTAP**. The observed HR-MALDI-FT-ICR-MS spectrum and CHN elemental analysis data provided a reasonable match with a compound whose molecular formula is $\text{C}_{98}\text{H}_{110}\text{N}_8\text{O}_2\text{P}$, constituting a TAP phosphorus complex without any ion, suggesting that **rPTAP** is a one-electron reduced neutral radical. **rPTAP** is extremely air- and photo-stable, such that a glovebox system is unnecessary for the entire synthetic process. Moreover, the absorption spectrum remained unchanged when **rPTAP** was stored as a solid in air under ambient light for more than 1 year.

To confirm the redox properties of **rPTAP**, cyclic voltammograms of **PTAP** and **rPTAP** were measured in *o*-dichlorobenzene (*o*-DCB) (not shown). Since the redox potentials can be shifted anodically by insertion of a phosphorus(V) atom into the azaporphyrin

core, the redox waves of **PTAP** appeared at only slightly less than 0 V vs Fc^+/Fc . Interestingly, the voltammogram of **rPTAP** is compatible with that of **PTAP**, showing five redox waves at similar positions to the redox waves of **PTAP**, indicating that **rPTAP** has very close redox behavior to **PTAP** and is a good multiple electron acceptor. For assignment of the redox relationship between **rPTAP** and **PTAP**, spectroelectrochemical measurements in *o*-DCB were performed. When a potential negative enough for the first reduction reaction to occur was applied to the solution of **PTAP** (Fig. 28a), new weak bands appeared in the near-IR region, while the bands in the UV-vis region broadened, accompanying a set of clear isosbestic points. The final absorption spectrum fully matched the absorption spectrum of an as-prepared **rPTAP** solution. When the applied potential was returned to 0 V, the original spectrum was regenerated. More importantly, when a potential positive enough for the first oxidation reaction to occur was applied to the solution of as-prepared **rPTAP** (Fig. 28b), the final absorption spectrum fully matched the absorption spectrum of **PTAP** and the changes were reversible. In summary, the spectroelectrochemical switching between **PTAP** and **rPTAP** was completely reversible, supporting the premise that **rPTAP** is an air-stable one-electron reduced species of **PTAP**.

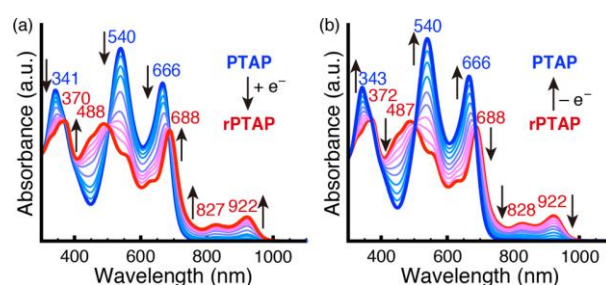


Fig. 28. (a) Spectral changes of **PTAP** solution by applying -0.2 V potential vs Ag/AgCl reference electrode in *o*-DCB. (b) Spectral changes of **rPTAP** solution by applying 0.3 V potential vs Ag/AgCl reference electrode in *o*-DCB

Рис. 28. (a) Изменения спектров раствора **PTAP** при приложении потенциала $-0,2$ В относительно электрода сравнения Ag / AgCl в *o*-DCB. (b) Изменения спектра раствора **rPTAP** при приложении потенциала $0,3$ В по сравнению с электродом сравнения Ag / AgCl в *o*-DCB

The solid state structure of **rPTAP** was unambiguously elucidated by X-ray diffraction analysis of crystals obtained from a toluene solution of **rPTAP** (Fig. 29). The phosphorus atom sits in the center of the 4N mean plane ($\Delta 4\text{N} < 0.005 \text{ \AA}$), and the macrocycle is highly planar ($\Delta r = 0.06$), although the reported structures of TAP or Pc phosphorus(V) complexes are ruffled, due to the small atomic radius (98 pm) of the phosphorus atom. Indeed, the bond lengths between phosphorus and the pyrrole-nitrogen in **rPTAP** are longer than those of **PTAP**. More interestingly, two

kinds of P–N bond lengths were found (1.8654(14) and 1.8745(14) Å) for **rPTAP**, while all P–N bond lengths in **PTAP** are the same (1.839(2) Å), indicating that the chromophore symmetry has been slightly altered. The HOMA indexes for the internal cross in **rPTAP** and **PTAP** are 0.84 and 0.90, respectively. Hence no significant bond-length alternation was observed for the C–N bonds even in the core structure of **rPTAP**, similarly as for those of **PTAP** (a typical 18 π aromatic molecule).

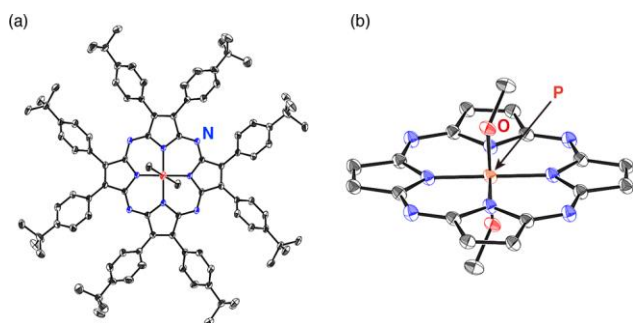


Fig. 29. X-ray crystal structure of **rPTAP**. The thermal ellipsoids were scaled to the 50% probability level. (a) Top view; (b) side view (peripheral substituents are omitted). In both views, hydrogen atoms have been omitted for clarity

Рис. 29. Рентгеновская кристаллическая структура **rPTAP**. Тепловые эллипсоиды масштабированы до уровня вероятности 50%. а) вид сверху; (б) вид сбоку (периферийные заместители опущены). В обоих представлениях атомы водорода опущены для ясности

However, the EPR spectra of **rPTAP** in 1.0 and 0.1 mM solution in degassed CH_2Cl_2 showed a singlet with $g = 2.01$ and 2.001 , respectively, characteristic of a delocalized radical having an unpaired electron ($S = 1/2$); no hyperfine coupling to nitrogen atoms was observed even in diluted and degassed solution (as per similar Pc^{3-} systems). The VT ^1H NMR spectrum of **rPTAP** in toluene- d_8 was also measured (not shown). No peaks were found in the normal region for aromatic protons (ca. 6–9 ppm). However, broad signals were observed at low-field (10.7 and 18.0 ppm at 298 K), which could be assigned to paramagnetically shifted aryl protons of the peripheral substituents. A reversible temperature dependence was also observed between 298 and 353 K whereby the two peaks shift linearly toward the diamagnetic region with higher temperature, reaching 10.2 and 17.7 ppm at 353 K, consistent with **rPTAP** containing an unpaired electron. The ^{31}P NMR signal for **rPTAP** is a simple very broad (approximately 25 ppm) peak centered at -233 ppm; its extreme broadness is consistent with the paramagnetism. Finally, the spin density distribution of the model compound **rPTAP'**, where the peripheral substituents of **rPTAP** were replaced by phenyl groups, was calculated. The calculations implied the unpaired electron density to be encompassed over the TAP macrocycle, as well as no spin-density at the central phosphorus. Furthermore, the calculated positive charge on

the central phosphorus was unchanged between **PTAP'** and **rPTAP'**, confirming the valence of the phosphorus center in **rPTAP** to be +5.

All electrochemical, spectroscopic, and theoretical results support the premise that the valence of the **rPTAP** macrocyclic core is -3 and that the complete **rPTAP** molecule is an air-stable neutral radical. With this air-stable, reduced azaporphyrinoid in hand, the absorption properties of -3 azaporphyrins could be investigated unambiguously. Here, partial MO energy diagrams of **rPTAP'** and the calculated stick absorption spectrum are shown in Fig. 30. An MCD spectrum also gives information on the electronic structure of azaporphyrin, so that the detailed absorption and MCD spectra of **rPTAP** are shown in Fig. 31. It was proposed in a previous report [45] that the ground state of -3 Pcs was distorted from D_{4h} symmetry to C_{2v} symmetry due to Jahn-Teller effects.

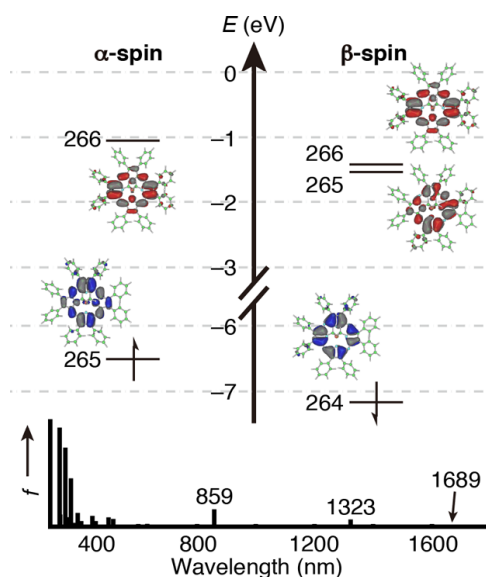


Fig. 30. Partial molecular energy diagrams and orbitals of **rPTAP'** (top) and its calculated absorption spectrum (bottom). Calculations were performed at the ULC-BLYP/6-31G**/UB3LYP/6-31G* level

Рис. 30. Диаграммы парциальной молекулярной энергии и орбитали **rPTAP'** (вверху) и рассчитанный спектр поглощения (внизу). Расчеты проводились на уровне ULC-BLYP / 6-31G* // UB3LYP / 6-31G*

Indeed, the bond lengths between phosphorus and the pyrrole nitrogens in the X-ray crystallographic structure are slightly altered. In the MCD spectrum at longer wavelengths, relatively weak and strong Faraday B terms were observed at 933 and 883 nm, corresponding to the absorption band at 915 nm, reflecting the altered structure. An intense Faraday B term appeared at 698 nm, so that the change of orbital angular momentum between the ground and excited states for the absorption band at 681 nm appears to be larger than for other bands. Theoretical calculations for the -3 TAP ligand also support the experimental results. Although

many orbitals contribute to the calculated low-energy bands, in each band we could find mainly contributing one $\pi \rightarrow \pi^*$ transition. The SOMO (265A) \rightarrow LUMO (266A) intrashell transition was estimated to lie beyond 1500 nm (1689 nm); however, this transition should be forbidden, which may not appear in the experimental spectra. The HOMO (264B) \rightarrow LUMO (265B or 266B) transitions were estimated at 1323 and 859 nm, which are allowed transitions from $M_L = \pm 4$ to ± 5 . The properties of the calculated bands and MCD spectra support the assignment of the absorption bands at 915 and 681 nm to $\pi \rightarrow \pi^*$ bands calculated at 1323 and 859 nm, respectively. The corresponding occupied and unoccupied orbitals are delocalized on the TAP core, without localization at peripheral phenyl rings.

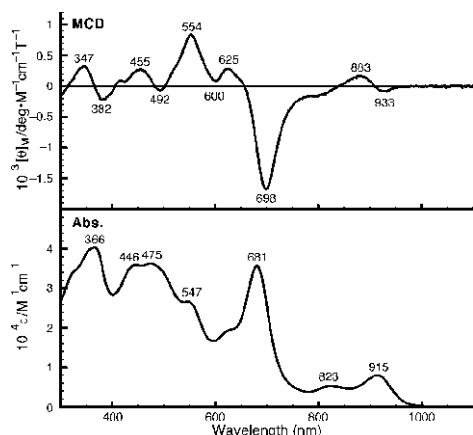


Fig. 31. UV-vis-NIR absorption (bottom) and MCD (top) spectra of **rPTAP** in CH_2Cl_2

Рис. 31. Спектры поглощения в ультрафиолетовой и инфракрасной областях спектра (внизу) и MCD (вверху) **rPTAP** в CH_2Cl_2

In summary, an extremely air-stable 19π -electron azaporphyrin has been prepared and characterized; it was easily obtained from the reduction of a cationic phosphorus-containing complex of TAP. The central phosphorus(V) atom and peripheral bulky groups may be crucial to stabilize the reduced state. VT-NMR and EPR spectra support the premise that the unpaired electron is delocalized on the TAP macrocycle. Finally, analysis of absorption and MCD spectra, together with theoretical calculations concluded that **rPTAP** is the first example of an isolated -3 TAP complex, namely, a 19π or $(4n+3)\pi$ azaporphyrinoid.

ACKNOWLEDGEMENT

This work was partly supported by Grant-in-Aid for Scientific Research (C), No. 18K05076, from the JSPS.

REFERENCES ЛИТЕРАТУРА

- Zhou Z., Chang Y., Shimizu S., Mack J., Schutt C., Herges R., Shen Z., Kobayashi N. Core-Modified Rubyrins Containing Dithienylethene Moieties. *Angew. Chem. Int. Ed.* 2014. V. 53. P. 6563-6567.
- Geuenich D., Hess K., Kçhler F., Herges R. Anisotropy of the Induced Current Density (ACID), a General Method To Quantify and Visualize Electronic Delocalization. *Chem. Rev.* 2005. V. 105. P. 3758–3772.
- Lee S., You Y., Ohkubo K., Fukuzumi S., Nam W. Photoelectrocatalysis to Improve Cycloreversion Quantum Yields of Photochromic Dithienylethene Compounds. *Angew. Chem. Int. Ed.* 2012. V. 51. P. 13154–13158.
- Wu V., Descalzo A. B., Weik F., Emmerling F., Shen Z., You X.-Z., Rurack K. A Core-Modified Rubyrin with meso-Aryl Substituents and Phenanthrene-Fused Pyrrole Rings: A Highly Conjugated Near-Infrared Dye and Hg^{2+} Probe. *Angew. Chem. Int. Ed.* 2008. V. 47. P. 193–197.
- Lindsey J.S., Schreiman I.C., Hsu H.C., Kearney P.C., Marguerettaz A.M. Rothmund and Adler-Longo Reactions Revisited: Synthesis of Tetraphenylporphyrins under Equilibrium Conditions. *J. Org. Chem.* 1987. V. 52. P. 827–836.
- Michl J. Magnetic Circular Dichroism of Cyclic π -electron Systems. 2. Algebraic Solution of the Perimeter Model for the B Terms of Systems with a $(4N+2)\pi$ -Electron $[n]$ Annulene Perimeter. *J. Am. Chem. Soc.* 1978. V. 100. P. 6812-6818.
- Muranaka A., Homma S., Maeda H., Furuta H., Kobayashi N. Detection of unusual $\Delta\text{HOMO} < \Delta\text{LUMO}$ relationship in tetrapyrrolic cis- and trans-doubly N-confused porphyrins. *Chem. Phys. Lett.* 2008. V. 460. P. 495-498.
- Howeler U., Downing J.W., Fleischhauer J., Michl J. MCD of Non-Aromatic Cyclic π -Electron Systems. Part 1. The Perimeter Model for Antiaromatic $4n$ -Electron $[n]$ Annulene Biradicals. *J. Chem. Soc. Perkin Trans.* 1998. V. 2. P. 1101–1117.
- Fleischhauer J., Howeler M.U., Michl J. Magnetic Circular Dichroism of Non-Aromatic Cyclic π -Electron Systems. 2. [1] The Perimeter Model for High-Symmetry ‘Unaromatic’ and ‘Ambiaromatic’ Molecules Derived from $4n$ -Electron $[n]$ Annulenes. *Spectrochim. Acta Part A.* 1999. V. 55. P. 585–606.
- Fleischhauer J., Howeler U., Michl J. MCD of Nonaromatic Cyclic π -Electron Systems. 3. The Perimeter Model for Low-Symmetry ‘Unaromatic’ and ‘Ambiaromatic’ Molecules Derived from $4n$ -Electron $[n]$ Annulenes. *J. Phys. Chem. A.* 2000. V. 104. P. 7762–7775.
- Fleischhauer J., Michl J. MCD of Nonaromatic Cyclic π -Electron Systems. 4. Explicit Relations between Molecular Structure and Spectra. *J. Phys. Chem. A.* 2000. V. 104. P. 7776–7784.
- Mack J., Stillman M.J., Kobayashi N. Application of MCD Spectroscopy to Porphyrinoids. *Coord. Chem. Review.* 2007. V. 251. P. 429-453.
- Kobayashi N. Muranaka A., Mack J. Circular Dichroism and Magnetic Circular Dichroism for Organic Chemists (textbook). London: Royal Society of Chemistry, 2012. (comments in *Angew. Chem. Int. Ed.* 2012. V. 51. P. 10446).
- Matshushita O., Derkacheva V.M., Muranaka A., Shimizu S., Uchiyama M., Luk'yanets E.A., Kobayashi N. Rectangular-Shaped Expanded Phthalocyanines with Two Central Metal Atoms. *J. Am. Chem. Soc.* 2012. V. 134. P. 3411-3418.
- Engel M.K. Single Crystal Structures of Phthalocyanine Complexes and Related Macrocycles. In ‘The Porphyrin Handbook’. Ed. by K.M. Kadish, K.M. Smith, R. Guilard. New York: Academic Press. 2003. V. 20. Chap. 122. P. 1-242.
- Kobayashi N. Synthesis and Spectroscopic Properties of Phthalocyanine Analogues. In ‘Handbook of Porphyrins and Related Macrocycles’. Ed. by K.M. Kadish, K.M. Smith, R. Guilard. New York: Academic Press. 2002. V. 15. Chap. 100. P. 161-262.
- (a) Moser F.H., Thomas A.L. The Phthalocyanines, Boca Raton, FL: CRC Press. 1983. V. I & II. b) Leznoff C.C. Synthesis of Metal-Free Substituted Phthalocyanines. In ‘Phthalocyanines: Properties and Applications’. Ed. by C.C. Leznoff, A.B.P. Lever. New York: VCH. 1989. V. 1. Chap. 1. P. 1-54. c) Nemykin V.N., Luk'yanets E.A. The Key Role of Peripheral Substituents in the Chemistry of Phthalocyanines. In ‘Handbook of Porphyrin Science’. Ed. by K.M. Kadish, K.M. Smith, R. Guilard. Singapore: World Scientific. 2010. V. 3. Chap. 11.

18. **Modéc B., Sala M., Clerac R.** Pyrazine-Assisted Dimerization of Molybdenum(V): Synthesis and Structural Characterization of Novel Dinuclear and Tetranuclear Complexes. *Eur. J. Inorg. Chem.* 2010. V. 2010. N 4. P. 542–553.
19. **Mizutani J., Imoto H., Saito H.** Tetrafluoroborate Salt of Tricarbonyl(2-methoxy- η^5 -cyclohexadienyl)iron(II). *Acta Crystallogr.* 1997. V. C53. P. 47–50.
20. **Gorsch M., Kienast A., Huckstadt H., Homborg V.** High Intensity Trip-Multiplet Transitions, a Reality! Synthesis, Properties, and Crystal Structure of 1-Bis(triphenylphosphine)iminium trans-Dibromophthalocyaninato(2–)molybdate(III). *Z. Anorg. Allg. Chem.* 1997. V. 623. P. 1433–1440.
21. **Frick K., Verma S., Sundermeyer J.** Novel Nitrido- and Oxo(phthalocyaninato) Complexes of Molybdenum, Tungsten and Rhenium. *Eur. J. Inorg. Chem.* 2000. V. 5. P. 1025–1030.
22. **Fukuda T., Makarova E.A., Luk'yanets E.A., Kobayashi N.** Synthesis and Spectroscopic and Electrochemical Studies of Novel Benzo- or 2,3-Naphtho-Fused Tetraaza-chlorins, -bacteriochlorins, and -isobacteriochlorins. *Chem. Eur. J.* 2004. V. 10. P. 117–133.
23. **Kobayashi N., Nakajima S., Ogata H., Fukuda T.** Synthesis, Spectroscopy, and Electrochemistry of Tetra-*tert*-Butylated Tetraazaporphyrins, Phthalocyanines, Naphthalocyanines, and Anthracocyanines, together with Molecular Orbital Calculations. *Chem. Eur. J.* 2004. V. 10. P. 6294–6312.
24. (a) **Kobayashi N., Fukuda T.** First Observation of the Vibrational Circular Dichroism Spectra of Synthetic Chiral Porphyrines. *Chem. Lett.* 2004. V. 33. P. 32–33. (b) **Makarova E.A., Fukuda T., Luk'yanets E.A., Kobayashi N.** Synthesis, Spectroscopic, and Electrochemical Studies of 1,2-Naphthalene-Ring-Fused Tetraaza-chlorins, -bacteriochlorins, and -isobacteriochlorins: The Separation and Characterization of Structural Isomers. *Chem. Eur. J.* 2005. V. 11. P. 1235–1250.
25. (a) **Nyokong T.** The Oxidation of Oxomolybdenum Phthalocyanine. *Inorg. Chim. Acta.* 1989. V. 160. P. 235–239. (b) **Nyokong T.** Cyclic Voltammetry and Photooxidation of Molybdenum Phthalocyanine. *Polyhedron* 1994. V. 13. P. 215–220.
26. A ^{14}N NMR spectrum was recorded for **2** (not shown). The signal was measured between –1000 and 800 ppm, but only a single peak was observed at –66 ppm. If the structure of **2** were consistent with that of **5B** in its core structure, at least two ^{14}N NMR peaks would be anticipated. Although the ^1H NMR data can be interpreted for both structures **5A** and **5B** (Fig. 6), this result also supports the characterization of **2** as **5A**.
27. **Gouterman M.** In *The Porphyrins*. Ed. by D. Dolphin. New York: Academic Press. 1978. V. 3. Chap. 1.
28. **Mack J., Stillman M.J.** Electronic Structures of Metal Phthalocyanine and Porphyrin Complexes from Analysis of the UV-Visible Absorption and Magnetic Circular Dichroism Spectra and Molecular Orbital Calculations. In “The Porphyrin Handbook”. Ed. by K.M. Kadish, K.M. Smith, R. Guilard. New York: Academic Press. 2003. V. 16. Chap. 103. P. 43–116.
29. **Muranaka A., Matsushita O., Yoshida K., Mori S., Suzuki M., Furuyama T., Uchiyama M., Osuka A., Kobayashi N.** Application of the Perimeter Model to the Assignment of the Electronic Absorption Spectra of Gold(III) Hexaphyrins with $[4n+2]$ and $[4n]$ π -Electron Systems. *Chem. Eur. J.* 2009. P. 15. P. 3744–3751.
30. **Michl J.** Electronic Structure of Aromatic π -Electron Systems as Reflected in Their MCD Spectra. *Pure Appl. Chem.* 1980. V. 52. P. 1549–1563.
31. **Furuyama T., Sato T., Kobayashi N.** A Bottom-up Synthesis of Antiaromatic Expanded Phthalocyanines: Pentabenzotriazasamaragdyrins, i.e. Norcorroles of Superphthalosyanines. *J. Am. Chem. Soc.* 2015. V. 137. P. 13788–13791.
32. (a) **Mack J., Sosa-Vargas L., Coles S.J., Tizzard G.J., Chamberier I., Cammidge A.N., Cook M.J., Kobayashi N.** Synthesis, Characterization, MCD Spectroscopy, and TD-DFT Calculations of Copper Metalated Nonperipherally Substituted Octa-Octyl Derivatives of Tetrabenzotriazaporphyrin, cis and trans Tetrabenzodiazaporphyrin, Tetrabenzomonoazaporphyrin, and Tetrabenzoporphyrin. *Inorg. Chem.* 2012. V. 51. P. 12820–12833. (b) **Leznoff C.C., McKeown N.B.** Preparation of Substituted Tetrabenzotriazaporphyrins and a Tetranaphthotriazaporphyrin: A Route to Mono-meso-Substituted Phthalocyanine Analogs. *J. Org. Chem.* 1990. V. 55. P. 2186–2190.
33. **Elvidge J.A., Golden J.H.** Compounds Containing Directly Linked Pyrrole Rings. Part II. Dialkylimino- β -isoidindigos. *J. Chem. Soc.* 1956. P. 4144–4150.
34. **Mori H., Sung Y.M., Lee B.S., Kim D., Osuka A.** Antiaromatic Hexaphyrins and Octaphyrins Stabilized by the Hydrogen-Bonding Interactions of meso-Imidazolyl Groups. *Angew. Chem., Int. Ed.* 2012. V. 51. P. 12459–12463.
35. **Furuyama T., Ogura Y., Yoza K., Kobayashi N.** Superazaporphyrins: Meso-Pentaazapentaphyrins and One of Their Low-Symmetry Derivatives. *Angew. Chem. Int. Ed.* 2012. V. 51. P. 11110–11114.
36. **Ito T., Hayashi Y., Shimizu S., Shin J.-Y., Kobayashi N., Shinokubo H.** Gram-Scale Synthesis of Nickel(II) Norcorrole: The Smallest Antiaromatic Porphyrinoid. *Angew. Chem., Int. Ed.* 2012. V. 51. P. 8542–8545.
37. a) **Okujima T., Jin G., Matsumoto N., Mack J., Mori S., Ohara K., Kuzuhara D., Ando C., Ono N., Yamada H., Uno H., Kobayashi N.** Cyclo[8]isoidindoles: Ring-Expanded and Annulated Porphyrinoids. *Angew. Chem., Int. Ed.* 2011. V. 50. P. 5699–5703. b) **Kuzuhara D., Mack J., Yamada H., Okujima T., Ono N., Kobayashi N.** Synthesis, Structures, and Optical and Electrochemical Properties of Benzoporphycenes. *Chem. Eur. J.* 2009. V. 15. P. 10060–10069.
38. **Okujima T., Ando C., Mack J., Mori S., Hisaki I., Nakae T., Yamada H., Ohara K., Kobayashi N., Uno H.** Acenaphthylene-Fused Cyclo[8]pyrroles with Intense Near-IR-Region Absorption Bands. *Chem. Eur. J.* 2013. V. 19. P. 13970–13978.
39. **Okujima T., Ando C., Agrawal S., Matsumoto H., Mori S., Ohara K., Hisaki I., Nakae T., Takase M., Uno H., Kobayashi N.** Template Synthesis of Decaphyrin without Meso-Bridges: Cyclo[10]pyrrole. *J. Am. Chem. Soc.* 2016. V. 138. P. 7540–7543.
40. a) **Seidel D., Lynch V., Sessler J.L.** Cyclo[8]pyrrole: A Simple-to-Make Expanded Porphyrin with No Meso Bridges. *Angew. Chem. Int. Ed.* 2002. V. 41. P. 1422–1425. b) **Gorski A., Köhler T., Seidel D., Lee J. T., Orzanowska G., Sessler J. L., Waluk.** Electronic Structure, Spectra, and Magnetic Circular Dichroism of Cyclohexa-, Cyclohepta-, and Cyclooctapyrrole. *Chem. Eur. J.* 2005. V. 11. P. 4179–4184.
41. **Ito S., Uno H., Murashima T., Ono N.** Synthesis, Properties and Crystal Structures of Rigid Porphyrins Fused with Bicyclo[2.2.2]octene Units. *Chem. Commun.* 1999. P. 2275–2276.
42. **Kobayashi N., Nakai K.** Applications of Magnetic Circular Dichroism Spectroscopy to Porphyrins and Phthalocyanines. *Chem. Commun. (Feature Article)*. 2007. P. 4077–4092.
43. **Muranaka A., Matsushita O., Yoshida K., Mori S., Suzuki M., Furuyama T., Uchiyama M., Osuka A., Kobayashi N.** Application of the Perimeter Model to the Assignment of the Electronic Absorption Spectra of Gold(III) Hexaphyrins with $[4n+2]$ and $[4n]$ π -Electron Systems. *Chem. Eur. J.* 2008. V. 15. P. 3744–3751.
44. **Yoshida T., Zhou W., Furuyama T., Leznoff D.B., Kobayashi N.** An Extremely Air-Stable 19π Porphyrinoid. *J. Am. Chem. Soc.* 2015. V. 137. P. 9258–9261.
45. **Mack J., Stillman M.J.** Photochemical Formation of the Anion Radical of Zinc Phthalocyanine and Analysis of the Absorption and Magnetic Circular Dichroism Spectral Data. Assignment of the Optical Spectrum of $[\text{ZnPc}(-3)]^-$. *J. Am. Chem. Soc.* 1994. V. 116. P. 1292–1304.

Поступила в редакцию (Received) 05.04.2019
Принята к опубликованию (Accepted) 08.06.2019